

Channeling of spontaneous emission from an atom into the fundamental and higher-order modes of a vacuum-clad ultrathin optical fiber

Fam Le Kien, S. Sahar S. Hejazi, and Thomas Busch

Quantum Systems Unit, Okinawa Institute of Science and Technology Graduate University, Onna, Okinawa 904-0495, Japan

Viet Giang Truong

Light-Matter Interactions Unit, Okinawa Institute of Science and Technology Graduate University, Onna, Okinawa 904-0495, Japan

Sile Nic Chormaic

Light-Matter Interactions Unit, Okinawa Institute of Science and Technology Graduate University, Onna, Okinawa 904-0495, Japan and

School of Chemistry and Physics, University of KwaZulu-Natal, Durban, KwaZulu-Natal, 4001, South Africa

(Dated: October 15, 2020)

We study spontaneous emission from a rubidium atom into the fundamental and higher-order modes of a vacuum-clad ultrathin optical fiber. We show that the spontaneous emission rate depends on the magnetic sublevel, the type of modes, the orientation of the quantization axis, and the fiber radius. We find that the rate of spontaneous emission into the TE modes is always symmetric with respect to the propagation directions. Directional asymmetry of spontaneous emission into other modes may appear when the quantization axis does not lie in the meridional plane containing the position of the atom. When the fiber radius is in the range from 330 nm to 450 nm, the spontaneous emission into the HE₂₁ modes is stronger than into the HE₁₁, TE₀₁, and TM₀₁ modes. At the cutoff for higher-order modes, the rates of spontaneous emission into guided and radiation modes undergo steep variations, which are caused by the changes in the mode structure. We show that the spontaneous emission from the upper level of the cyclic transition into the TM modes is unidirectional when the quantization axis lies at an appropriate azimuthal angle in the fiber transverse plane.

I. INTRODUCTION

Optical fibers can be tapered to a diameter comparable to or smaller than the wavelength of light [1–3]. Due to the tapering, the original core almost vanishes and the refractive indices that determine the guiding properties of the tapered fiber are those of the original silica cladding and the surrounding vacuum. Since the diameters of such tapered fibers are in the range of a few hundred nanometers, they are usually called nanofibers. When the radius of the fiber is small enough, it can support only a single mode in the optical region of frequency.

In a vacuum-clad nanofiber, the guided field penetrates an appreciable distance into the surrounding medium and appears as an evanescent wave carrying a significant fraction of the power and having a complex polarization pattern [4–6]. Nanofibers are therefore versatile tools for coupling light and matter and have a wide range of potential practical applications [7, 8]. For example, they have been used for trapping atoms [9–11], for probing atoms [12–20], molecules [21], quantum dots [22], and color centers in nanodiamonds [23, 24], and for mechanical manipulation of small particles [25–27].

Tapered fibers can also be fabricated with slightly larger diameters or larger refractive indices so that they can support not only the fundamental HE₁₁ mode but also several higher-order modes. Compared to the HE₁₁ mode, the higher-order modes have larger cutoff size parameters and more complex intensity, phase, and polar-

ization distributions. For ease of reference, the vacuum-clad tapered fibers that can support the fundamental mode and several higher-order modes are called ultrathin optical fibers in this paper.

It has been shown that ultrathin optical fibers with higher-order modes can be used to trap, probe, and manipulate atoms, molecules, and particles [28–34]. The excitation of higher-order modes has been studied [35, 36]. The production of ultrathin fibers with higher-order modes [37–39] and the experimental studies on the interaction with atoms [40] or particles [41, 42] have been reported. The possibility to control and manipulate individual atoms near an ultrathin fiber can also find applications for quantum information.

The interaction between guided light and atoms is of academic and practical interest. Many applications require a deep understanding and an effective control of spontaneous emission of atoms near an ultrathin optical fiber. Radiative decay of an atom in the vicinity of a nanofiber has been studied in the context of a two-level atom [43–45] as well as a realistic multilevel atom with a hyperfine structure of energy levels [46, 47]. The parameters for the decay of populations [43–47] and cross-level coherences [46–48] have been calculated.

Recently, emission of particles with circularly polarized dipoles began to attract much attention [49–57]. It has been shown that the near-field interference of a circularly polarized dipole coupled to a dielectric or metallic object leads to unidirectional excitation of guided modes

or surface plasmon polariton modes [49–55]. This effect has been experimentally demonstrated by shining circularly polarized light onto a nanoslit [49, 51] or closely spaced subwavelength apertures [50] in a metal film and by exciting a nanoparticle on a dielectric interface with a tightly focused vector light beam [54, 55].

It has been shown that spontaneous emission and scattering from an atom with a circular dipole near a nanofiber can be asymmetric with respect to the opposite axial propagation directions [58–63]. These directional effects are the signatures of spin-orbit coupling of light [64–68] carrying transverse spin angular momentum [66, 69]. They are due to the existence of a nonzero longitudinal component of the nanofiber guided field, which oscillates in phase quadrature with respect to the radial transverse component. The possibility of directional emission from an atom into propagating radiation modes of a nanofiber and the possibility of generation of a lateral force on the atom have been reported [62]. The direction-dependent emission and absorption of photons lead to chiral quantum optics [70].

Spontaneous emission from a multilevel atom into the fundamental and higher-order modes of an ultrathin fiber has been studied by Masalov and Minogin [71]. They have found that the decay rates into the higher-order modes can be significantly larger than into the fundamental mode. Their calculations were limited to single transitions and single polarizations. However, all types of transitions and polarizations must be accounted for in a realistic situation. In addition, in Ref. [71] the fiber axis was used as the quantization axis and consequently no direction dependencies of the rates could be observed. Moreover, emission into radiation modes was not considered in Ref. [71].

The aim of the present paper is to investigate directional spontaneous emission from a multilevel atom with an arbitrary quantization axis into an ultrathin fiber. We calculate the rates of spontaneous emission into the fundamental and higher-order guided modes propagating in a given direction. We also calculate the rate of spontaneous emission into radiation modes.

The paper is organized as follows. In Sec. II we describe the interaction of an alkali-metal atom with the electromagnetic field in the presence of an ultrathin optical fiber. Section III is devoted to the basic characteristics of spontaneous emission of the multilevel atom. In Sec. IV we present numerical results. Our conclusions are given in Sec. V.

II. MODEL AND HAMILTONIAN

We consider a multilevel alkali-metal atom trapped in the vicinity of a vacuum-clad ultrathin optical fiber [see Fig. 1(a)]. We use Cartesian coordinates $\{x, y, z\}$, where z is the coordinate along the fiber axis, and also cylindrical coordinates $\{r, \varphi, z\}$, where r and φ are the polar coordinates in the fiber transverse plane xy . The energy

levels of the atom are specified in a Cartesian coordinate system $\{x_Q, y_Q, z_Q\}$, where z_Q is the direction of the quantization axis.

To be concrete, we assume that the atom is ^{87}Rb . We work with the D_2 line of the rubidium atom, which corresponds to the electric dipole transition from the excited state $5P_{3/2}$ to the ground state $5S_{1/2}$ [see Fig. 1(b)] [72]. We introduce the notations $|e\rangle = |J'F'M'\rangle$ and $|g\rangle = |JFM\rangle$ for the magnetic sublevels of the hyperfine-structure (hfs) levels of the excited state and the ground state, respectively. Here, J and J' are the total electronic angular momenta, F and F' are the total atomic angular momenta, and M and M' are the magnetic quantum numbers. We denote the energies of these sublevels as $\hbar\omega_e$ and $\hbar\omega_g$. The schematic of the hfs levels of the D_2 line of the rubidium-87 atom is illustrated in Fig. 1(b).

We introduce the notation $\mathbf{d}_{eg} = \langle e|\mathbf{D}|g\rangle$ for the dipole matrix element of the transition $|e\rangle \leftrightarrow |g\rangle$, where \mathbf{D} is the electric dipole operator. In the atomic quantization coordinate system $\{x_Q, y_Q, z_Q\}$, the spherical components $q = 0, \pm 1$ of the dipole matrix element \mathbf{d}_{eg} are given by the expression [73]

$$d_{qQ} = (-1)^{I+J'-M'} \langle J' \| D \| J \rangle \sqrt{(2F+1)(2F'+1)} \\ \times \begin{Bmatrix} J' & F' & I \\ F & J & 1 \end{Bmatrix} \begin{pmatrix} F & 1 & F' \\ M & q & -M' \end{pmatrix}. \quad (1)$$

Here, the array in the curly braces is a $6j$ symbol, the array in the parentheses is a $3j$ symbol, I is the nuclear spin, and $\langle J' \| D \| J \rangle$ is the reduced electric dipole matrix element in the J basis. Note that d_{qQ} is nonzero only for $M' - M = q = 0, \pm 1$.

We assume that the fiber has a cylindrical silica core of radius a and refractive index n_1 and an infinite vacuum cladding of refractive index $n_2 = 1$. We retain the silica dispersion and at the frequency of the rubidium D_2 line the refractive index n_1 of the fiber is taken as 1.4537. The positive-frequency part $\mathbf{E}^{(+)}$ of the electric component of the field can be decomposed into the contributions $\mathbf{E}_g^{(+)}$ and $\mathbf{E}_r^{(+)}$ from guided and radiation modes, respectively, as

$$\mathbf{E}^{(+)} = \mathbf{E}_g^{(+)} + \mathbf{E}_r^{(+)}. \quad (2)$$

In view of the very low losses of silica in the wavelength range of interest, we neglect material absorption.

We follow the continuum field quantization procedures presented in [74]. Regarding the guided modes, we assume that the fiber supports the fundamental HE_{11} mode and a few higher-order modes [75] in a finite bandwidth around the central frequency $\omega_0 = \omega_e - \omega_g$ of the rubidium-87 D_2 line. We label each guided mode in this bandwidth by an index $\mu = (\omega, N, f, p)$. Here, ω is the mode frequency, the notation $N = \text{HE}_{lm}, \text{EH}_{lm}, \text{TE}_{0m}$, or TM_{0m} stands for the mode type, with $l = 1, 2, \dots$ and $m = 1, 2, \dots$ being the azimuthal and radial mode orders, respectively, and the index $f = +1$ or -1 denotes respectively the forward or backward propagation direction along the fiber axis z . The HE_{lm} and EH_{lm} modes

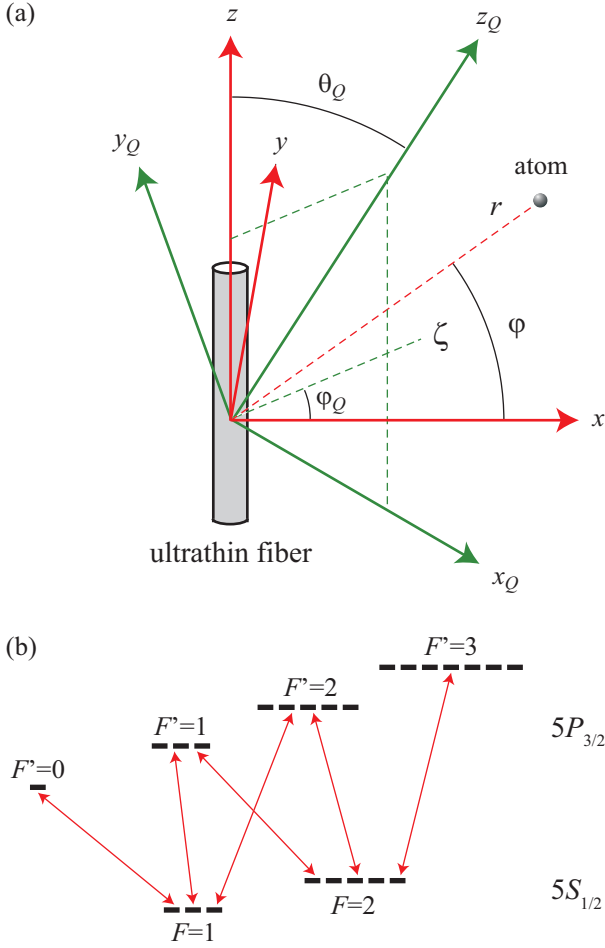


FIG. 1. (Color online) (a) An atom interacting with guided and radiation modes of an ultrathin optical fiber. The fiber-based Cartesian coordinate system $\{x, y, z\}$, the corresponding cylindrical coordinate system $\{r, \varphi, z\}$, and the quantization coordinate system $\{x_Q, y_Q, z_Q\}$ are used. (b) Schematic of the hfs levels of the $5P_{3/2}$ and $5S_{1/2}$ states of a rubidium-87 atom. These levels are specified with respect to the quantization axis z_Q .

are hybrid modes. For these modes, the azimuthal order is $l \neq 0$, and the index p is equal to $+1$ or -1 , indicating the counterclockwise or clockwise circulation direction of the helical phasefront. The TE_{0m} and TM_{0m} modes are transverse electric and magnetic modes. For these modes, the azimuthal mode order is $l = 0$ and hence, the mode polarization is single and the polarization index p can take an arbitrary value. For convenience, we assign the value $p = 0$ to the polarization index p for TE_{0m} and TM_{0m} modes. In the interaction picture, the quantum expression for the positive-frequency part $\mathbf{E}_g^{(+)}$ of the electric component of the field in guided modes is [46]

$$\mathbf{E}_g^{(+)} = i \sum_{\mu} \sqrt{\frac{\hbar\omega\beta'}{4\pi\epsilon_0}} a_{\mu} \mathbf{e}^{(\mu)} e^{-i(\omega t - f\beta z - p l \varphi)}. \quad (3)$$

Here, $\mathbf{e}^{(\mu)} = \mathbf{e}^{(\mu)}(r, \varphi)$ is the profile function of the guided mode μ in the classical problem, a_{μ} is the corresponding photon annihilation operator, $\sum_{\mu} = \sum_{Nfp} \int_0^{\infty} d\omega$ is the generalized summation over the guided modes, β is the longitudinal propagation constant, and β' is the derivative of β with respect to ω . The constant β is determined by the fiber eigenvalue equation [75]. The operators a_{μ} and a_{μ}^{\dagger} satisfy the continuous-mode bosonic commutation rules $[a_{\mu}, a_{\mu'}^{\dagger}] = \delta(\omega - \omega') \delta_{NN'} \delta_{ff'} \delta_{pp'}$. In deriving Eq. (3), we have used the normalization condition

$$\int_0^{2\pi} d\varphi \int_0^{\infty} n_{\text{ref}}^2 |\mathbf{e}^{(\mu)}|^2 r dr = 1, \quad (4)$$

where $n_{\text{ref}}(r) = n_1$ for $r < a$ and n_2 for $r > a$.

The explicit expressions for the profile functions $\mathbf{e}^{(\mu)}$ of guided modes are given in Refs. [75, 76] and are summarized in Appendix A. For a hybrid mode $N = HE_{lm}$ and EH_{lm} with the propagation direction f and the phase circulation direction p , the profile function is given in the cylindrical coordinates as

$$\mathbf{e}^{(\omega Nfp)}|_{N=HE_{lm}, EH_{lm}} = e_r \hat{\mathbf{r}} + p e_{\varphi} \hat{\boldsymbol{\varphi}} + f e_z \hat{\mathbf{z}}, \quad (5)$$

where e_r , e_{φ} , and e_z are given by Eqs. (A10) and (A11) for $\beta > 0$ and $l > 0$. For a TE_{0m} mode with the propagation direction f , the profile function can be written as

$$\mathbf{e}^{(\omega TE_{0m}f)} = \mathbf{e}^{(\omega TE_{0m}fp)}|_{p=0} = e_{\varphi} \hat{\boldsymbol{\varphi}}, \quad (6)$$

where the only nonzero cylindrical component e_{φ} is given by the second expressions in Eqs. (A17) and (A18). For a TM mode with the propagation direction f , we have

$$\mathbf{e}^{(\omega TM_{0m}f)} = \mathbf{e}^{(\omega TM_{0m}fp)}|_{p=0} = e_r \hat{\mathbf{r}} + f e_z \hat{\mathbf{z}}, \quad (7)$$

where the components e_r and e_z are given by the first and third expressions in Eqs. (A22) and (A23) for $\beta > 0$. An important property of the mode functions of hybrid and TM modes is that the longitudinal component e_z is nonvanishing and in quadrature ($\pi/2$ out of phase) with the radial component e_r .

In the case of radiation modes, the longitudinal propagation constant β for each value of the frequency ω can vary continuously, from $-k$ to k (with $k = \omega/c$). We label each radiation mode by an index $\nu = (\omega, \beta, l, p)$, where $l = 0, \pm 1, \pm 2, \dots$ is the mode order and $p = +, -$ is the mode polarization. In the interaction picture, the quantum expression for the positive-frequency part $\mathbf{E}_r^{(+)}$ of the electric component of the field in radiation modes is [46]

$$\mathbf{E}_r^{(+)} = i \sum_{\nu} \sqrt{\frac{\hbar\omega}{4\pi\epsilon_0}} a_{\nu} \mathbf{e}^{(\nu)} e^{-i(\omega t - \beta z - l \varphi)}. \quad (8)$$

Here, $\mathbf{e}^{(\nu)} = \mathbf{e}^{(\nu)}(r, \varphi)$ is the profile function of the radiation mode ν in the classical problem, a_{ν} is the corresponding photon annihilation operator, and $\sum_{\nu} =$

$\sum_{lp} \int_0^\infty d\omega \int_{-k}^k d\beta$ is the generalized summation over the radiation modes. The operators a_ν and a_ν^\dagger satisfy the continuous-mode bosonic commutation rules $[a_\nu, a_{\nu'}^\dagger] = \delta(\omega - \omega')\delta(\beta - \beta')\delta_{ll'}\delta_{pp'}$. In deriving Eq. (8), we have used the normalization condition

$$\int_0^{2\pi} d\varphi \int_0^\infty n_{\text{ref}}^2 \left[\mathbf{e}^{(\nu)} \mathbf{e}^{(\nu')*} \right]_{\beta=\beta', l=l', p=p'} r dr = \delta(\omega - \omega'). \quad (9)$$

The explicit expressions for the mode functions $\mathbf{e}^{(\nu)}$ are given in Refs. [75, 76] and are summarized in Appendix B.

Assume that the atom is positioned at a point (r, φ, z) . The Hamiltonian for the atom-field interaction in the dipole and rotating-wave approximations is given by

$$H_{\text{int}} = -i\hbar \sum_{\alpha eg} G_{\alpha eg} \sigma_{ge}^\dagger a_\alpha e^{-i(\omega - \omega_{eg})t} + \text{H.c.}, \quad (10)$$

where the notations $\alpha = \mu, \nu$ and $\sum_\alpha = \sum_\mu + \sum_\nu$ stand for the general mode index and the complete mode summation, respectively, and the operators $\sigma_{ge} = |g\rangle\langle e|$ and $\sigma_{ge}^\dagger = \sigma_{eg} = |e\rangle\langle g|$ describe the downward and upward transitions, respectively. The coefficients

$$G_{\mu eg} = \sqrt{\frac{\omega\beta'}{4\pi\epsilon_0\hbar}} (\mathbf{d}_{eg} \cdot \mathbf{e}^{(\mu)}) e^{i(f\beta z + pl\varphi)},$$

$$G_{\nu eg} = \sqrt{\frac{\omega}{4\pi\epsilon_0\hbar}} (\mathbf{d}_{eg} \cdot \mathbf{e}^{(\nu)}) e^{i(\beta z + l\varphi)} \quad (11)$$

characterize the coupling of the atomic transition $e \leftrightarrow g$ with the guided mode μ and the radiation mode ν . The notation $\omega_{eg} = \omega_e - \omega_g$ stands for the atomic transition frequency.

We note that, for $|e\rangle = |J'F'M'\rangle$ and $|g\rangle = |JFM\rangle$, the scalar product of the atomic dipole vector \mathbf{d}_{eg} and the field vector $\mathbf{e}^{(\alpha)}$ can be expressed as $\mathbf{d}_{eg} \cdot \mathbf{e}^{(\alpha)} = (-1)^q d_{qQ} e_{-qQ}^{(\alpha)}|_{q=M'-M}$, where d_{qQ} is given by Eq. (1) and $e_{qQ}^{(\alpha)}$ is the corresponding spherical tensor component of the field in the atomic quantization coordinate system $\{x_Q, y_Q, z_Q\}$. The components $e_{qQ}^{(\alpha)}$ with $q = 0, \pm 1$ are defined as $e_{-1Q}^{(\alpha)} = (e_{xQ}^{(\alpha)} - ie_{yQ}^{(\alpha)})/\sqrt{2}$, $e_{0Q}^{(\alpha)} = e_{zQ}^{(\alpha)}$, and $e_{1Q}^{(\alpha)} = -(e_{xQ}^{(\alpha)} + ie_{yQ}^{(\alpha)})/\sqrt{2}$. Let θ_Q be the angle between the quantization axis z_Q and the fiber axis z [see Fig. 1(a)]. Assume that the plane (z, z_Q) intersects with the fiber transverse plane xy at a line ζ . Let φ_Q be the azimuthal angle between ζ and x . We choose the axes x_Q and y_Q such that x_Q is in the plane (z_Q, z) and y_Q is in the plane (x, y) . Then, the transformation for the field vector $\mathbf{e}^{(\alpha)}$ from the coordinate system $\{x, y, z\}$ to the coordinate system $\{x_Q, y_Q, z_Q\}$ is given by the equations

$$\begin{aligned} e_{xQ}^{(\alpha)} &= (e_x^{(\alpha)} \cos \varphi_Q + e_y^{(\alpha)} \sin \varphi_Q) \cos \theta_Q - e_z^{(\alpha)} \sin \theta_Q, \\ e_{yQ}^{(\alpha)} &= -e_x^{(\alpha)} \sin \varphi_Q + e_y^{(\alpha)} \cos \varphi_Q, \\ e_{zQ}^{(\alpha)} &= (e_x^{(\alpha)} \cos \varphi_Q + e_y^{(\alpha)} \sin \varphi_Q) \sin \theta_Q + e_z^{(\alpha)} \cos \theta_Q. \end{aligned} \quad (12)$$

The relations between the Cartesian-coordinate vector components $e_x^{(\alpha)}$ and $e_y^{(\alpha)}$ and the cylindrical-coordinate vector components $e_r^{(\alpha)}$ and $e_\varphi^{(\alpha)}$ are $e_x^{(\alpha)} = e_r^{(\alpha)} \cos \varphi - e_\varphi^{(\alpha)} \sin \varphi$ and $e_y^{(\alpha)} = e_r^{(\alpha)} \sin \varphi + e_\varphi^{(\alpha)} \cos \varphi$.

III. SPONTANEOUS EMISSION OF THE ATOM

In this section, we study spontaneous emission of the multilevel atom. We assume that the field is initially in the vacuum state $|0\rangle$. In this case, the time evolution of the reduced density operator ρ of the atom is governed by the equations [46]

$$\begin{aligned} \dot{\rho}_{ee'} &= -\frac{1}{2} \sum_{e''} (\gamma_{ee''} \rho_{e''e'} + \gamma_{e''e'} \rho_{ee''}), \\ \dot{\rho}_{gg'} &= \sum_{ee'} \gamma_{e'eg'g} \rho_{ee'}, \\ \dot{\rho}_{eg} &= -\frac{1}{2} \sum_{e'} \gamma_{ee'} \rho_{e'g}, \end{aligned} \quad (13)$$

where the coefficients

$$\begin{aligned} \gamma_{ee'gg'} &= \gamma_{ee'gg'}^{(g)} + \gamma_{ee'gg'}^{(r)}, \\ \gamma_{ee'} &= \sum_g \gamma_{ee'gg} = \gamma_{ee'}^{(g)} + \gamma_{ee'}^{(r)} \end{aligned} \quad (14)$$

characterize the spontaneous emission process. In Eqs. (14), the set of coefficients $\gamma_{ee'gg'}^{(g)}$ and $\gamma_{ee'}^{(g)}$ describes spontaneous emission into guided modes, and the set of coefficients $\gamma_{ee'gg'}^{(r)}$ and $\gamma_{ee'}^{(r)}$ describes spontaneous emission into radiation modes. The expressions for these coefficients are given as [46]

$$\begin{aligned} \gamma_{ee'gg'}^{(g)} &= 2\pi \sum_{Nfp} G_{Nfp} G_{Nfp}^* G_{Nfp}^* G_{Nfp}, \\ \gamma_{ee'}^{(g)} &= \sum_g \gamma_{ee'gg}^{(g)}, \end{aligned} \quad (15)$$

and

$$\begin{aligned} \gamma_{ee'gg'}^{(r)} &= 2\pi \sum_{lp} \int_{-k_0 n_2}^{k_0 n_2} d\beta G_{\beta l p e g} G_{\beta l p e' g'}^*, \\ \gamma_{ee'}^{(r)} &= \sum_g \gamma_{ee'gg}^{(r)}, \end{aligned} \quad (16)$$

where $G_{Nfp} \equiv G_{\omega_0 Nfp}$ and $G_{\beta l p e g} \equiv G_{\omega_0 \beta l p e g}$ are the coupling coefficients for the resonant guided and radiation modes, respectively.

The diagonal decay coefficients $\gamma_e^{(g)} \equiv \gamma_{ee}^{(g)}$ and $\gamma_e^{(r)} \equiv \gamma_{ee}^{(r)}$ are the rates of spontaneous emission from the magnetic sublevel $|e\rangle$ of the atom into guided and radiation modes, respectively. The total decay rate for the population of the sublevel $|e\rangle$ is

$$\gamma_e \equiv \gamma_{ee} = \gamma_e^{(g)} + \gamma_e^{(r)}. \quad (17)$$

The rate of spontaneous emission from the magnetic sublevel $|e\rangle$ of the atom into the guided modes $N = \text{HE}_{lm}, \text{EH}_{lm}, \text{TE}_{0m},$ or TM_{0m} is given by

$$\gamma_e^{(N)} = 2\pi \sum_{fpg} |G_{Nfpeg}|^2. \quad (18)$$

It is clear that

$$\gamma_e^{(g)} = \sum_N \gamma_e^{(N)} = 2\pi \sum_{Nfpg} |G_{Nfpeg}|^2. \quad (19)$$

We note that the density-matrix equations (13) are in agreement with those used in the treatments for the excitation of a multilevel atom by light of arbitrary polarization [48, 77–82]. Equations (13) can, in principle, be used for an arbitrary (degenerate and nondegenerate) multilevel atom. The tensor nature of the Zeeman sublevels and the hfs levels of a realistic alkali-metal atom is expressed by Eq. (1) for the spherical tensor components of the atomic dipole matrix elements \mathbf{d}_{eg} . These quantities enter Eqs. (13) through expressions (11) for the coupling coefficients $G_{\mu eg}$ and $G_{\nu eg}$. Unlike the case of the atom-field system in free space [48], the presence of the nanofiber modifies the decay rates γ_e and leads to the appearance of the cross-level decay coefficients $\gamma_{ee'}$ (with $e \neq e'$) in Eqs. (13) (see [46]).

We introduce the notation

$$\gamma_{eg}^{(Nfp)} = 2\pi |G_{Nfpeg}|^2, \quad (20)$$

which stands for the rate of spontaneous emission into the guided modes Nfp via the transition $|e\rangle \rightarrow |g\rangle$. The rate of spontaneous emission from the sublevel $|e\rangle$ of the atom into the guided modes N with the propagation direction f is given by

$$\gamma_e^{(Nf)} = \sum_{pg} \gamma_{eg}^{(Nfp)}. \quad (21)$$

The rate of spontaneous emission into all types of guided modes propagating in the direction f is given by

$$\gamma_e^{(gf)} = \sum_N \gamma_e^{(Nf)}. \quad (22)$$

For TE modes, the profile function for the electric part of the field does not depend on the propagation direction f [see Eq. (6)]. Therefore, the rates $\gamma_e^{(Nf)}$ for $N = \text{TE}$ modes is symmetric with respect to f .

For hybrid and TM modes, the longitudinal component $e_z^{(\omega Nfp)}$ of the field is nonvanishing and has opposite signs for opposite propagation directions [see Eqs. (5) and (7)]. Therefore, the rates $\gamma_e^{(Nf)}$ for $N = \text{HE}, \text{EH},$ and TM modes and the rate $\gamma_e^{(gf)}$ for all guided modes may depend on f .

The rates $\gamma_e^{(Nf)}$ and hence $\gamma_e^{(gf)}$ do not depend on f when the quantization axis z_Q coincides with the fiber axis z . Indeed, in this case, we have $e_{qQ}^{(\omega Nfp)} = e_q^{(\omega Nfp)}$

for $q = 0, \pm 1$, where $e_q^{(\omega Nfp)}$ are the spherical tensor components of the mode function $\mathbf{e}^{(\omega Nfp)}$ in the fiber coordinate system $\{x, y, z\}$. These components satisfy the relation

$$e_q^{(\omega Nfp)} = (-1)^{1+q} e_q^{(\omega N\bar{f}p)}, \quad (23)$$

where $\bar{f} = -f$. Hence, we find the relation

$$G_{Nfpeg} = (-1)^{1+M'-M} G_{N\bar{f}peg} e^{2if\beta z}, \quad (24)$$

which yields $\gamma_{eg}^{(Nfp)} = \gamma_{eg}^{(N\bar{f}p)}$ and, hence, $\gamma_e^{(N+)} = \gamma_e^{(N-)}$ and $\gamma_e^{(g+)} = \gamma_e^{(g-)}$.

More generally, we find that $\gamma_e^{(Nf)}$ and hence $\gamma_e^{(gf)}$ do not depend on f when the quantization axis z_Q lies in the meridional plane containing the position of the atom. In order to show this directional independence, we assume that the atom is on the x axis and the quantization axis z_Q lies in the zx plane, that is, $\varphi_Q = 0$. Then, for hybrid and TM modes with the profile functions (5) and (7), Eqs. (12) yield

$$\begin{aligned} e_{xQ}^{(\mu)} &= e_r \cos \theta_Q - f e_z \sin \theta_Q, \\ e_{yQ}^{(\mu)} &= p e_\varphi, \\ e_{zQ}^{(\mu)} &= e_r \sin \theta_Q + f e_z \cos \theta_Q. \end{aligned} \quad (25)$$

According to Appendix A, for an appropriate choice of the normalization constant, e_z and e_φ are real numbers and e_r is an imaginary number. Hence, we can show that the absolute values $|e_{qQ}^{(\mu)}|$ of the spherical tensor components of the field in the coordinate system $\{x_Q, y_Q, z_Q\}$ do not depend on f . On the other hand, the dipole matrix element \mathbf{d}_{eg} has a single nonzero spherical tensor component d_{qQ} , which is a real number. Consequently, the absolute value of the scalar product $\mathbf{d}_{eg} \cdot \mathbf{e}^{(\mu)}$ is $|\mathbf{d}_{eg} \cdot \mathbf{e}^{(\mu)}| = |d_{qQ}| |e_{-qQ}^{(\mu)}|$. This quantity is independent of f and, hence, so are the rates $\gamma_e^{(Nf)}$ and $\gamma_e^{(gf)}$.

It is worth noting that the rates $\gamma_e^{(N)}, \gamma_e^{(g)}, \gamma_e^{(r)}$, and γ_e are symmetric with respect to the magnetic quantum number M' of the sublevel $|e\rangle = |F'M'\rangle = |J'F'M'\rangle$, that is, $\gamma_e^{(N)} = \gamma_{\bar{e}}^{(N)}, \gamma_e^{(g)} = \gamma_{\bar{e}}^{(g)}, \gamma_e^{(r)} = \gamma_{\bar{e}}^{(r)}$, and $\gamma_e = \gamma_{\bar{e}}$, where the index \bar{e} labels the sublevel $|\bar{e}\rangle = |F', -M'\rangle$ with the opposite magnetic quantum number $-M'$. This symmetry is a consequence of the properties

$$\begin{aligned} \mathbf{e}^{(\omega, N, f, p)} &= -\mathbf{e}^{(\omega, N, -f, -p)*}, \\ \mathbf{e}^{(\omega, \beta, l, p)} &= (-1)^l \mathbf{e}^{(\omega, -\beta, -l, p)*}, \end{aligned} \quad (26)$$

and

$$\mathbf{d}_{eg} = (-1)^{F'-F+M'-M+1} \mathbf{d}_{\bar{e}\bar{g}}^*, \quad (27)$$

where $|\bar{g}\rangle = |F, -M\rangle$. With the help of the relations (26) and (27), we can also show that

$$\begin{aligned} \gamma_e^{(Nf)} &= \gamma_{\bar{e}}^{(N\bar{f})}, \\ \gamma_e^{(gf)} &= \gamma_{\bar{e}}^{(g\bar{f})}. \end{aligned} \quad (28)$$

Thus, the rates $\gamma_e^{(Nf)}$ and $\gamma_e^{(gf)}$ of spontaneous emission into guided modes propagating in a given direction f do not change when both the propagation direction f and the magnetic quantum number M' are reversed. It is clear that if $\gamma_e^{(Nf)}$ and $\gamma_e^{(gf)}$ depend on f then they also depend on the sign of M' and vice versa.

In order to get insight into the direction dependencies of the spontaneous emission rates, we consider the rate $\gamma_{eg}^{(Nf)} \equiv \sum_p \gamma_{eg}^{(Nfp)}$ for a given transition $|e\rangle \rightarrow |g\rangle$. When we follow the procedure of Ref. [83], we can decompose this rate as

$$\gamma_{eg}^{(Nf)} = \gamma_0^{(f)} + \gamma_1^{(f)} + \gamma_2^{(f)}, \quad (29)$$

where

$$\begin{aligned} \gamma_0^{(f)} &= \frac{\omega_0 \beta_0'}{6\epsilon_0 \hbar} |\mathbf{d}_{eg}|^2 \sum_p |\mathbf{e}^{(\omega_0 Nfp)}|^2, \\ \gamma_1^{(f)} &= \frac{\omega_0 \beta_0'}{4\epsilon_0 \hbar} [\mathbf{d}_{eg}^* \times \mathbf{d}_{eg}] \cdot \sum_p [\mathbf{e}^{(\omega_0 Nfp)*} \times \mathbf{e}^{(\omega_0 Nfp)}], \\ \gamma_2^{(f)} &= \frac{\omega_0 \beta_0'}{2\epsilon_0 \hbar} \{\mathbf{d}_{eg}^* \otimes \mathbf{d}_{eg}\}_2 \cdot \sum_p \{\mathbf{e}^{(\omega_0 Nfp)*} \otimes \mathbf{e}^{(\omega_0 Nfp)}\}_2. \end{aligned} \quad (30)$$

Here, the notation $\{\mathbf{A} \otimes \mathbf{B}\}_2$ stands for the irreducible tensor product of rank 2 of arbitrary complex vectors \mathbf{A} and \mathbf{B} . The quantities $\gamma_0^{(f)}$, $\gamma_1^{(f)}$, and $\gamma_2^{(f)}$ are called the scalar, vector, and tensor components of the rate $\gamma_{eg}^{(Nf)}$, respectively.

With the help of the first relation in Eqs. (26), we can show that $\gamma_0^{(f)} = \gamma_0^{(\bar{f})}$, $\gamma_1^{(f)} = -\gamma_1^{(\bar{f})}$, and $\gamma_2^{(f)} = \gamma_2^{(\bar{f})}$. Thus, the direction dependence of the rate $\gamma_{eg}^{(Nf)}$ occurs when the vector term $\gamma_1^{(f)}$ is nonvanishing.

According to the second expression in Eqs. (30), the vector term $\gamma_1^{(f)}$ depends on the overlap between the vectors $i[\mathbf{d}_{eg}^* \times \mathbf{d}_{eg}]$ and $-i[\mathbf{e}^{(\omega_0 Nfp)*} \times \mathbf{e}^{(\omega_0 Nfp)}]$, which are proportional to the ellipticity vector of the atomic electric dipole polarization and the ellipticity vector of the electric field polarization, respectively. The vector $i[\mathbf{d}_{eg}^* \times \mathbf{d}_{eg}]$ characterizes an effective magnetic dipole produced by the rotation of the electric dipole, and is responsible for the vector polarizability of the atom. The vector $-i[\mathbf{e}^{(\omega_0 Nfp)*} \times \mathbf{e}^{(\omega_0 Nfp)}]$ characterizes an effective magnetic field and is responsible for the local electric spin density of light. The vector component $\gamma_1^{(f)}$ of the rate can be considered as a result of the interaction between the effective magnetic dipole and the effective magnetic field. Due to spin-orbit coupling of light [64–68], a reverse of the propagation direction leads to a reverse of the spin density of light and, consequently, to a reverse of the vector component $\gamma_1^{(f)}$ of the spontaneous emission rate $\gamma_{eg}^{(Nf)}$.

We can show that $\sum_p [\mathbf{e}^{(\omega_0 Nfp)*} \times \mathbf{e}^{(\omega_0 Nfp)}] \propto f e_z e_r \hat{\varphi}$, which leads to $\gamma_1^{(f)} \propto f e_z e_r ([\mathbf{d}_{eg}^* \times \mathbf{d}_{eg}] \cdot \hat{\varphi})$. Hence, the

spontaneous emission rate $\gamma_{eg}^{(Nf)}$ depends on f only when the ellipticity vector $i[\mathbf{d}_{eg}^* \times \mathbf{d}_{eg}]$ of the atomic dipole has a nonvanishing azimuthal component $i[\mathbf{d}_{eg}^* \times \mathbf{d}_{eg}]_\varphi$. It is clear that the direction dependence of $\gamma_{eg}^{(Nf)}$ is a consequence of the fact that the longitudinal component e_z of the guided field is not zero.

IV. NUMERICAL RESULTS

In this section, we demonstrate the results of numerical calculations for the decay characteristics of the magnetic sublevels of the excited state $5P_{3/2}$ of a rubidium-87 atom in the presence of an ultrathin optical fiber. The atomic transitions between this state and the ground state $5S_{1/2}$ correspond to the D_2 line and have a wavelength $\lambda_0 = 780$ nm. For simplicity, we show only the results of calculations for the spontaneous emission rates γ_e of the sublevels $|e\rangle = |F'M'\rangle = |J'F'M'\rangle$ and their components.

A. Dependencies of the rates on the radial distance

In this subsection, we study the dependencies of the rates on the radial distance r . For simplicity, we consider the case where the fiber axis z is used as the quantization axis. In this case, none of the rates depend on the azimuthal angle φ . In addition, the decay rates of the sublevels with the magnetic quantum numbers M' and $-M'$ are the same.

We show in Fig. 2 the radial dependencies of the rates $\gamma_e^{(N)}$ of spontaneous emission from different magnetic sublevels of the hfs level $5P_{3/2}F' = 3$ of the rubidium atom into different guided modes. The fiber radius is chosen to be $a = 400$ nm. For the wavelength $\lambda_0 = 780$ nm, this fiber can support the HE_{11} , TE_{01} , TM_{01} , and HE_{21} modes. According to Fig. 2, the presence of the fiber leads to substantial decay rates into guided modes. Comparison between the different parts of the figure shows that the emission into the HE_{21} modes is stronger than into the HE_{11} , TE_{01} , and TM_{01} modes. We observe that different magnetic sublevels have different decay rates, unlike the case of alkali-metal atoms in free space. The rates of spontaneous emission from the outermost magnetic sublevels $|F' = 3, M' = \pm 3\rangle$ (red lines) into guided modes are larger than those from the other sublevels. This indicates that the polarization profiles of the guided modes are more favorable to the σ_\pm transitions than the π transition. The rates of spontaneous emission into guided modes are largest when the atom is positioned on the fiber surface. When the atom is far away from the fiber, $\gamma_e^{(N)}$ reduces to zero. Since the decay rates of the sublevels M' and $-M'$ are the same in the case where the quantization axis is the fiber axis, the maximum number of lines in each part of Fig. 2 is four. Since the difference between the decay rates for $M' = 0$ and $M' = \pm 1$ is

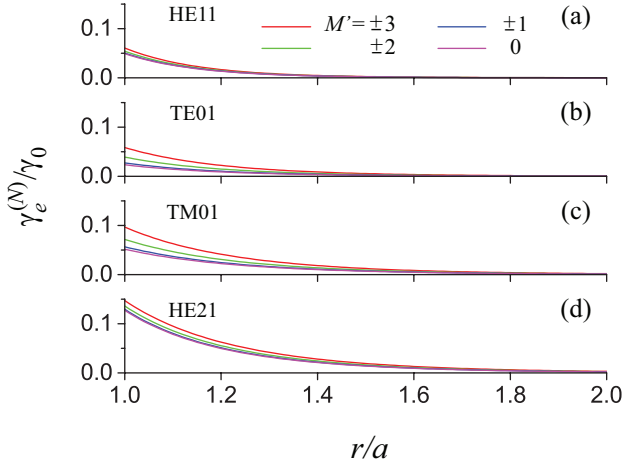


FIG. 2. (Color online) Radial dependencies of the rates $\gamma_e^{(N)}$ of spontaneous emission from different magnetic sublevels of the hfs level $5P_{3/2}F' = 3$ of a rubidium-87 atom into different guided modes of an ultrathin optical fiber. The quantization axis z_Q coincides with the fiber axis z . The fiber radius is $a = 400$ nm. The wavelength of the atomic transition is $\lambda_0 = 780$ nm. The refractive indices of the fiber and the vacuum cladding are $n_1 = 1.4537$ and $n_2 = 1$, respectively. The rates are normalized to the free-space decay rate γ_0 of the atom.

very small, we can clearly distinguish only three lines in Figs. 2(a) and 2(d).

We note that our results presented in Fig. 2 do not agree quantitatively with the results of Masalov and Minogin [71]. Indeed, the ratio between the rates of emission from the outermost levels into the HE₂₁ and HE₁₁ modes at the distance $r/a = 1$ is equal to about 3 in Fig. 2 but is equal to about 8 in the calculations of Ref. [71]. One of the reasons for the discrepancy is that they considered ^{85}Rb , while we study ^{87}Rb . Another reason is that they limited their calculations to atomic transitions and guided modes with a single type of polarization, while we include all atomic transitions and field modes in our treatment. The most important reason for the discrepancy is that Eq. (16) of Ref. [71] is not accurate.

We show in Fig. 3 the radial dependencies of the spontaneous emission rates $\gamma_e^{(g)}$, $\gamma_e^{(r)}$, and γ_e from different magnetic sublevels of the hfs level $5P_{3/2}F' = 3$ into guided modes, radiation modes, and both types of modes, respectively. We observe from Fig. 3(a) that the rates $\gamma_e^{(g)}$ for the outermost sublevels $M' = \pm 3$ (red lines) are larger than for the other sublevels. When the radial distance r is not too large, the rates $\gamma_e^{(r)}$ and γ_e for the sublevels $M' = \pm 3$ are also larger than for the other sublevels [see Figs. 3(b) and 3(c)]. When the atom is far away from the fiber, $\gamma_e^{(g)}$ reduces to zero [see Fig. 3(a)], while $\gamma_e^{(r)}$ and γ_e approach the free-space limiting value γ_0 [see Figs. 3(b) and 3(c)]. The small oscillations around the value of unity in Fig. 3(b) for $\gamma_e^{(r)}$ can be ascribed to the

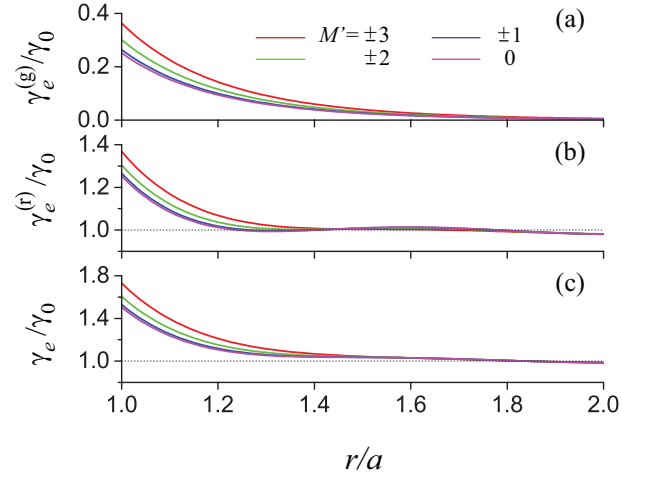


FIG. 3. (Color online) Radial dependencies of the rates $\gamma_e^{(g)}$, $\gamma_e^{(r)}$, and γ_e of spontaneous emission from different magnetic sublevels of the hfs level $5P_{3/2}F' = 3$ into (a) guided modes, (b) radiation modes, and (c) both types of modes. The parameters used are the same as for Fig. 2. The rates are normalized to the free-space decay rate γ_0 of the atom. The dotted lines stand for unity and are guides to the eye.

constructive and destructive interference due to reflections from the fiber surface [45]. Due to the interference, the total rate γ_e can become slightly smaller than γ_0 in some regions outside the fiber [see Fig. 3(c)].

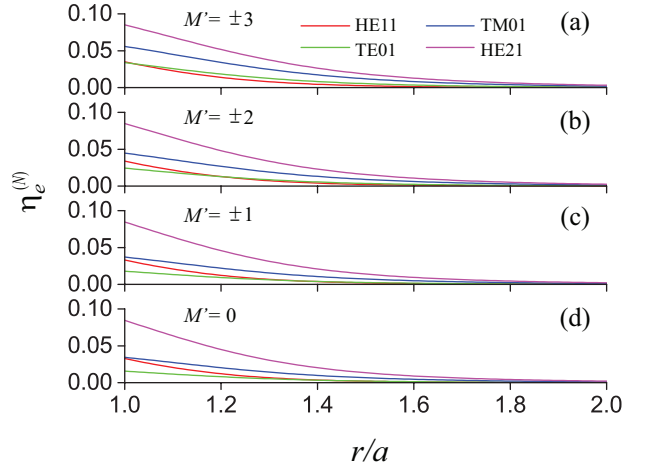


FIG. 4. (Color online) Radial dependencies of the fractional rates $\eta_e^{(N)} = \gamma_e^{(N)}/\gamma_e$ of spontaneous emission from different magnetic sublevels of the hfs level $5P_{3/2}F' = 3$ into different guided modes. The parameters used are the same as for Fig. 2.

We show in Fig. 4 the radial dependencies of the fractional rates $\eta_e^{(N)} = \gamma_e^{(N)}/\gamma_e$ of spontaneous emission from different magnetic sublevels of the hfs level $5P_{3/2}F' = 3$ into different guided modes. The figure shows that the fractional rates $\eta_e^{(N)}$ of emission from the sublevels into

the HE_{21} modes are larger than those into the HE_{11} , TE_{01} , and TM_{01} modes.

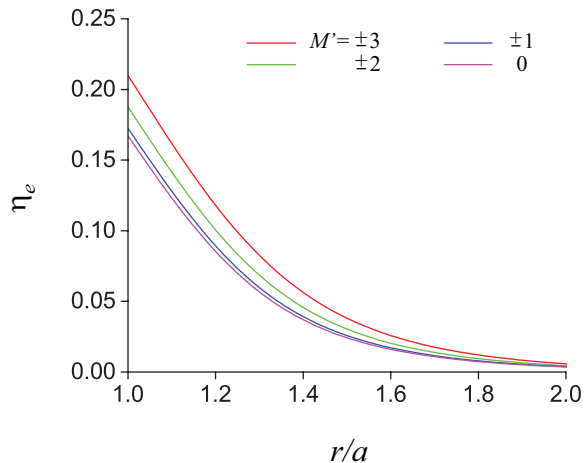


FIG. 5. (Color online) Radial dependencies of the fractional rates $\eta_e = \gamma_e^{(g)}/\gamma_e$ of spontaneous emission from different magnetic sublevels of the hfs level $5P_{3/2}F' = 3$ into all types of guided modes. The parameters used are the same as for Fig. 2.

We show in Fig. 5 the radial dependencies of the fractional rates $\eta_e = \gamma_e^{(g)}/\gamma_e = \sum_N \eta_e^{(N)}$ of spontaneous emission from different magnetic sublevels of the hfs level $5P_{3/2}F' = 3$ into all types of guided modes. The figure shows that the outermost sublevels $M' = \pm 3$ have the largest fractional rate. At the fiber surface, the fractional rates are largest. Their magnitudes are substantial, in the range from 0.17 to 0.21, depending on the magnetic quantum number M' .

Note that the hfs level $5P_{3/2}F' = 0$ is a singlet state, $|F' = 0, M' = 0\rangle$, which is equally coupled to the sublevels $|F = 1, M = 0, \pm 1\rangle$ of the hfs level $F = 1$ of the ground state $5S_{1/2}$. Therefore, the decay rate for the state $|F' = 0, M' = 0\rangle$ is equal to the average decay rate for an ensemble of two-level emitters with dipoles oriented randomly in space. We show in Fig. 6 the radial dependencies of the spontaneous emission rates $\gamma_e^{(g)}$, $\gamma_e^{(r)}$, and γ_e from the hfs level $5P_{3/2}F' = 0$ into guided modes, radiation modes, and both types of modes.

B. Dependencies of the rates on the fiber radius

In this subsection, we study the dependencies of the decay rates on the fiber radius a . We again use the fiber axis z as the quantization axis.

In Fig. 7, we show the rates $\gamma_e^{(N)}$ of spontaneous emission from different magnetic sublevels of the hfs level $5P_{3/2}F' = 3$ into different guided modes as functions of the fiber radius a . We observe from the figure that the rates $\gamma_e^{(N)}$ have maxima, whose positions and magnitudes strongly depend on the mode type N . The emis-

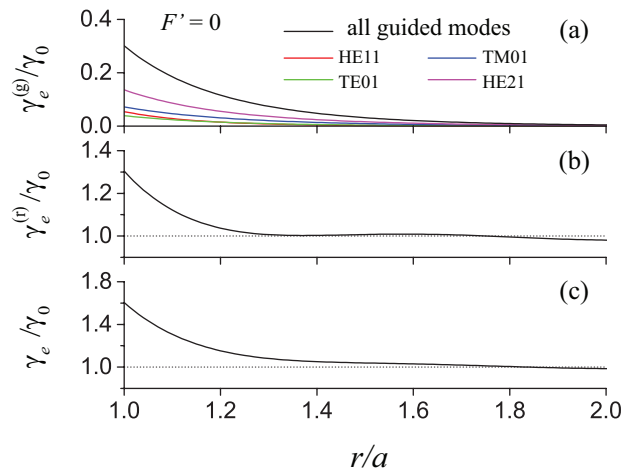


FIG. 6. (Color online) Radial dependencies of the rates $\gamma_e^{(g)}$, $\gamma_e^{(r)}$, and γ_e of spontaneous emission from the hfs level $5P_{3/2}F' = 0$ into (a) guided modes, (b) radiation modes, and (c) both types of modes. The components $\gamma_e^{(N)}$ of the rate $\gamma_e^{(g)}$ are also shown in part (a). The parameters used are the same as for Fig. 2. The rates are normalized to the free-space decay rate γ_0 of the atom. The dotted lines stand for unity and are guides to the eye.

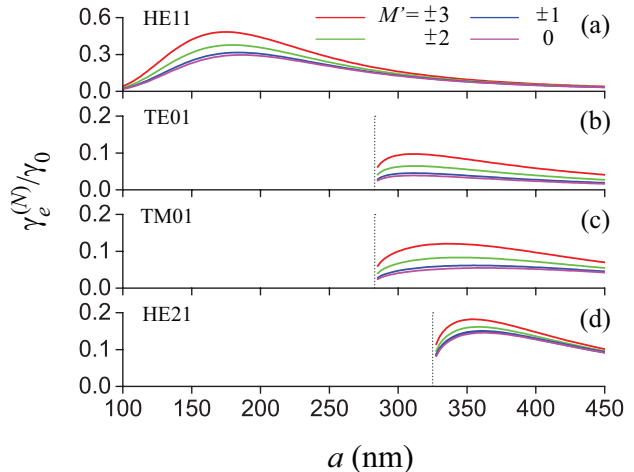


FIG. 7. (Color online) Rates $\gamma_e^{(N)}$ of spontaneous emission from different magnetic sublevels of the hfs level $5P_{3/2}F' = 3$ into different guided modes as functions of the fiber radius a . The atom is positioned on the fiber surface. Other parameters are as for Fig. 2. The rates are normalized to the free-space decay rate γ_0 of the atom. The vertical dotted lines indicate the positions of the cutoffs for higher-order modes.

sion from the atom into the fundamental HE_{11} modes is strongest when a is around 180 nm. For a given fiber radius a in the range from 330 nm to 450 nm (the sizes that are typically achieved experimentally), the emission into the HE_{21} modes is stronger than into the TM_{01} , TE_{01} , and HE_{11} modes. When the atom is positioned on the

fiber surface, the rates $\gamma_e^{(N)}$ for the outermost sublevels $M' = \pm 3$ are larger than for the other sublevels.

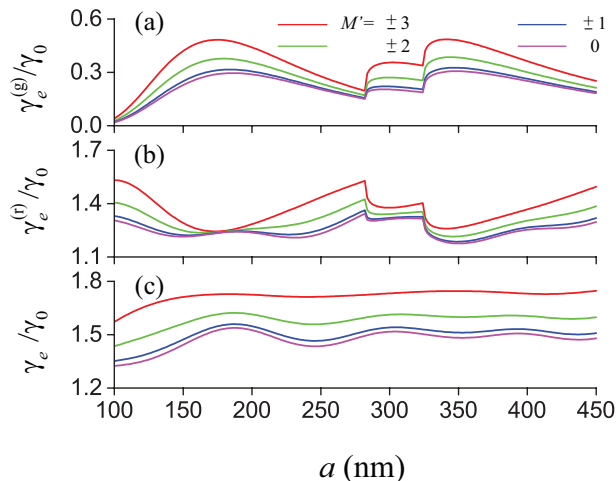


FIG. 8. (Color online) Rates $\gamma_e^{(g)}$, $\gamma_e^{(r)}$, and γ_e of spontaneous emission from different magnetic sublevels of the hfs level $5P_{3/2}F' = 3$ into (a) guided modes, (b) radiation modes, and (c) both types of modes as functions of the fiber radius a . The atom is positioned on the fiber surface. Other parameters are as for Fig. 2. The rates are normalized to the free-space decay rate γ_0 of the atom.

The rates $\gamma_e^{(g)}$, $\gamma_e^{(r)}$, and γ_e of spontaneous emission from different magnetic sublevels of the hfs level $5P_{3/2}F' = 3$ into guided modes, radiation modes, and both types of modes are shown as functions of the fiber radius a in Fig. 8. We observe from the figure that, in the case where the atom is positioned on the fiber surface, the rates $\gamma_e^{(g)}$, $\gamma_e^{(r)}$, and γ_e for the outermost magnetic sublevels $M' = \pm 3$ are larger than for the other sublevels. The dependencies of $\gamma_e^{(g)}$ and $\gamma_e^{(r)}$ on the fiber radius a are stronger than that of γ_e . The rates $\gamma_e^{(g)}$ and $\gamma_e^{(r)}$ undergo step variations at the point $a \simeq 283$ nm, which corresponds to the cutoff for the TE_{01} and TM_{01} modes, and at the point $a \simeq 325$ nm, which corresponds to the cutoff for the HE_{21} modes. Such abrupt changes are due to the changes of the mode structure at the cutoffs. It is interesting to note that the signs of the slopes of the changes of $\gamma_e^{(g)}$ and $\gamma_e^{(r)}$ at the cutoffs are opposite to each other. Due to the mutual compensation of these changes, the variations of the total decay rates γ_e at the cutoffs are smooth [see Fig. 8(c)].

We plot in Fig. 9 the fractional rates $\eta_e^{(N)} = \gamma_e^{(N)}/\gamma_e$ of spontaneous emission from different magnetic sublevels of the hfs level $5P_{3/2}F' = 3$ into different guided modes as functions of the fiber radius a . The figure shows clearly that the maximum value of $\eta_e^{(N)}$ for the HE_{11} modes is larger than for the TE_{01} , TM_{01} , and HE_{21} modes. For a given fiber radius in the range from 330 nm to 450 nm, the value of $\eta_e^{(N)}$ for the HE_{21} modes is larger than that for the other guided modes.

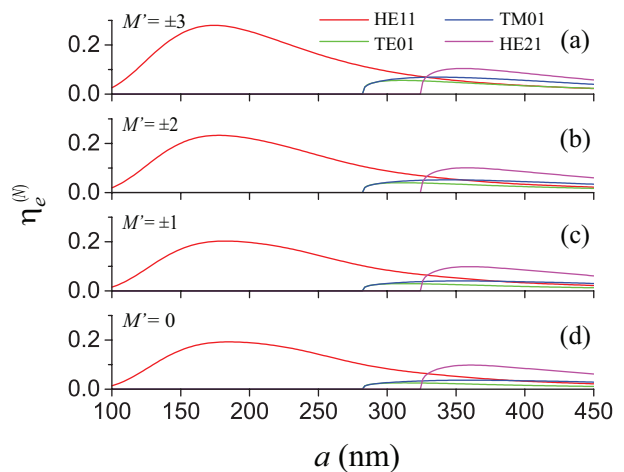


FIG. 9. (Color online) Fractional rates $\eta_e^{(N)} = \gamma_e^{(N)}/\gamma_e$ of spontaneous emission from different magnetic sublevels of the hfs level $5P_{3/2}F' = 3$ into different guided modes as functions of the fiber radius a . The atom is positioned on the fiber surface. Other parameters are as for Fig. 2.

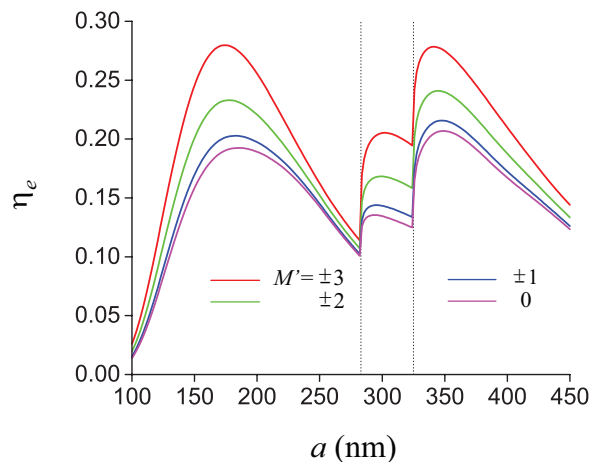


FIG. 10. (Color online) Fractional rates $\eta_e = \gamma_e^{(g)}/\gamma_e$ of spontaneous emission from different magnetic sublevels of the hfs level $5P_{3/2}F' = 3$ into guided modes as functions of the fiber radius a . The atom is positioned on the fiber surface. Other parameters are as for Fig. 2. The vertical dotted lines indicate the positions of the cutoffs for higher-order modes.

We show in Fig. 10 the fractional rates $\eta_e = \gamma_e^{(g)}/\gamma_e = \sum_N \eta_e^{(N)}$ of spontaneous emission from different magnetic sublevels of the hfs level $5P_{3/2}F' = 3$ into all types of guided modes as functions of the fiber radius a . The figure shows that the outermost magnetic sublevels $M' = \pm 3$ have the largest fractional rate. The fractional rates are most substantial when the fiber radius a is around 180 nm and 340 nm. Note that, for $a \simeq 180$ nm, the fiber supports only the fundamental HE_{11} modes, whereas, for $a \simeq 340$ nm, the fiber supports not only the HE_{11} modes but also the TE_{01} , TM_{01} , and

HE₂₁ modes.

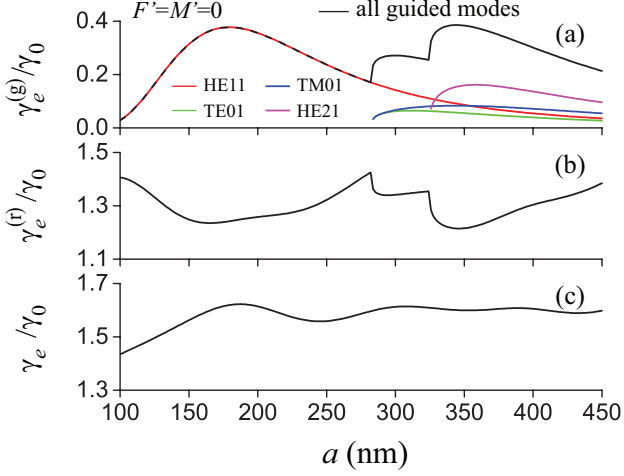


FIG. 11. (Color online) Rates $\gamma_e^{(g)}$, $\gamma_e^{(r)}$, and γ_e of spontaneous emission from the hfs level $5P_{3/2}F' = 0$ into (a) guided modes, (b) radiation modes, and (c) both types of modes as functions of the fiber radius a . The components $\gamma_e^{(N)}$ of the rate $\gamma_e^{(g)}$ are also shown in part (a). The atom is positioned on the fiber surface. Other parameters are as for Fig. 2. The rates are normalized to the free-space decay rate γ_0 of the atom.

We plot in Fig. 11 the spontaneous emission rates $\gamma_e^{(g)}$, $\gamma_e^{(r)}$, and γ_e from the hfs level $5P_{3/2}F' = 0$ into guided modes, radiation modes, and both types of modes as functions of the fiber radius. As already noted in the previous subsection, the decay rate for this hfs level is equal to the average decay rate of an ensemble of two-level emitters with dipoles oriented randomly in space. Figure 11 shows clearly that $\gamma_e^{(g)}$ and $\gamma_e^{(r)}$ vary significantly and steeply at the cutoffs, while the variations of γ_e are small and smooth.

C. Dependencies of the rates on the orientation of the quantization axis

The dipole matrix element \mathbf{d}_{eg} is a vector whose spherical tensor components are specified by Eq. (1) in the quantization coordinate system $\{x_Q, y_Q, z_Q\}$. It is clear that \mathbf{d}_{eg} depends on the orientation of the quantization axis z_Q and so do the scalar product $\mathbf{d}_{eg} \cdot \mathbf{e}^{(\alpha)}$ and, hence, the spontaneous emission rate for the transition between the sublevels $|e\rangle$ and $|g\rangle$. In the previous two subsections, we have studied the case where the quantization axis z_Q coincides with the fiber axis z . In this subsection, we examine the dependencies of the rates on the orientation of the quantization axis. For certainty, we assume that the atom is positioned on the axis x .

We plot in Figs. 12 and 13 the dependencies of the fractional rates η_e on the radial distance and the fiber radius for the quantization axis $z_Q = x$ and y . Comparison between parts (a) and (b) of these figures and

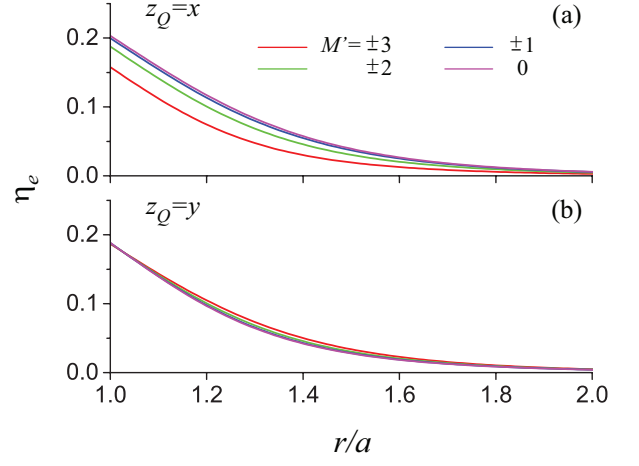


FIG. 12. (Color online) Radial dependencies of the fractional rates $\eta_e = \gamma_e^{(g)}/\gamma_e$ of spontaneous emission into guided modes for the quantization axis $z_Q = x$ (a) and y (b). The atom is positioned on the axis x . Other parameters are as for Fig. 2.

between these parts and Figs. 5 and 10 shows that the rates of spontaneous emission significantly depend on the orientation of the quantization axis. We observe that the spread of the rates with respect to the magnetic quantum number M' for $z_Q = y$ [see Figs. 12(b) and 13(b)] is smaller than for $z_Q = x$ [see Figs. 12(a) and 13(a)].

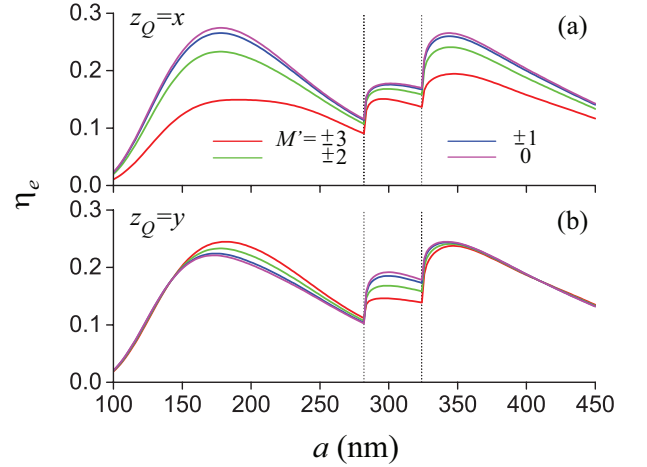


FIG. 13. (Color online) Fractional rates $\eta_e = \gamma_e^{(g)}/\gamma_e$ of spontaneous emission into guided modes for the quantization axis $z_Q = x$ (a) and y (b) as functions of the fiber radius a . The atom is positioned at the crossing between the fiber surface and the axis x . Other parameters are as for Fig. 2. The vertical dotted lines indicate the positions of the cutoffs for higher-order modes.

We plot in Figs. 14 and 15 the fractional rates η_e as functions of the azimuthal angle φ_Q and the zenithal angle θ_Q of the quantization axis z_Q . The figures show that the rates for the magnetic sublevels $|F' = 3, M' \neq \pm 2\rangle$

depend on the orientation of the quantization axis. It is interesting to note that the rate η_e for the sublevels $|F' = 3, M' = \pm 2\rangle$ (see the green curves) does not depend on φ_Q and θ_Q . This independence is a consequence of the $1/2/0$ ratio of the oscillatory strengths of the $\pi/\sigma_{\pm}/\sigma_{\mp}$ transitions from the magnetic sublevels $|F' = 3, M' = \pm 2\rangle$ [72]. The symmetry properties of the profile functions with respect to opposite propagation directions and opposite phase circulation directions also play an important role.

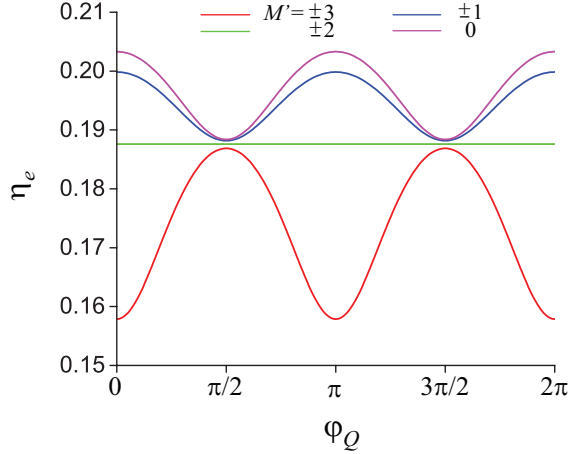


FIG. 14. (Color online) Fractional rates $\eta_e = \gamma_e^{(g)}/\gamma_e$ of spontaneous emission into guided modes as functions of the azimuthal angle φ_Q of the quantization axis z_Q . The zenithal angle of the axis z_Q is $\theta_Q = \pi/2$. The atom is positioned at the crossing between the fiber surface and the axis x . Other parameters are as for Fig. 2.

D. Directional spontaneous emission rates

It has been shown in Sec. III that, when the quantization axis z_Q coincides with the fiber axis z or, more generally, lies in the meridional plane containing the position of the atom, the spontaneous emission rates $\gamma_e^{(Nf)}$ and $\gamma_e^{(gf)}$ are symmetric with respect to the propagation direction f , that is, $\gamma_e^{(N+)} = \gamma_e^{(N-)}$ and $\gamma_e^{(g+)} = \gamma_e^{(g-)}$ [58]. However, when the quantization axis does not lie in the meridional plane containing the position of the atom, the decay rates $\gamma_e^{(Nf)}$ and $\gamma_e^{(gf)}$ may depend on the propagation direction f . In this subsection, we study the directional spontaneous emission rates for different choices of the quantization axis z_Q .

The directional fractional rates $\eta_e^{(f)} = \gamma_e^{(gf)}/\gamma_e$ for the positive ($f = +$) and negative ($f = -$) propagation directions are shown in Figs. 16 and 17 as functions of the radial distance and the fiber radius. In the calculations of these figures, we have assumed that the atom is positioned on the positive side of the axis x and the quantization axis z_Q coincides with the axis y . In Figs. 16 and

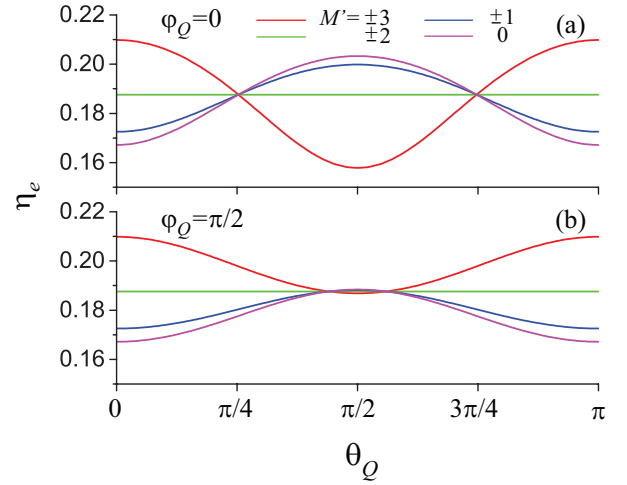


FIG. 15. (Color online) Fractional rates $\eta_e = \gamma_e^{(g)}/\gamma_e$ of spontaneous emission into guided modes as functions of the zenithal angle θ_Q of the quantization axis z_Q . The azimuthal angle of the axis z_Q is $\varphi_Q = 0$ (a) and $\pi/2$ (b). The atom is positioned at the crossing between the fiber surface and the axis x . Other parameters are as for Fig. 2.

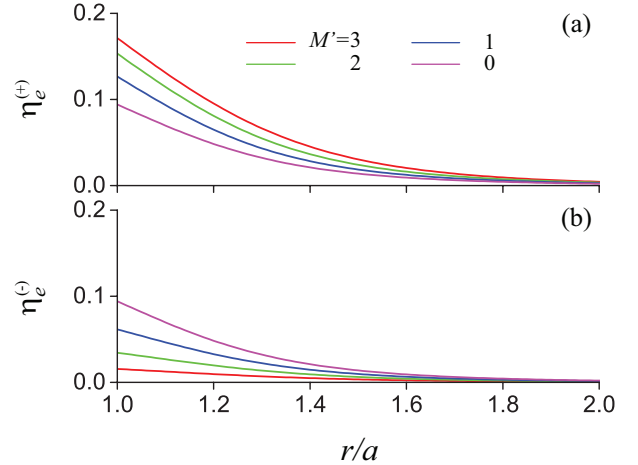


FIG. 16. (Color online) Radial dependencies of the directional fractional rates $\eta_e^{(f)} = \gamma_e^{(gf)}/\gamma_e$ of spontaneous emission into guided modes in the (a) positive and (b) negative propagation directions. The atom is positioned on the positive side of the axis x . The quantization axis z_Q coincides with the axis y . Other parameters are as for Fig. 2.

17, we do not show the factor $\eta_e^{(f)}$ for $M' < 0$ because it is equal to $\eta_e^{(f)}$ [see Eq. (24)]. Comparison between parts (a) and (b) of the figures shows that the directional factor $\eta_e^{(f)}$ has different values for different propagation directions except for the case $M' = 0$ (see the magenta curves).

The asymmetry between the directional rates of spontaneous emission into the positive and negative directions

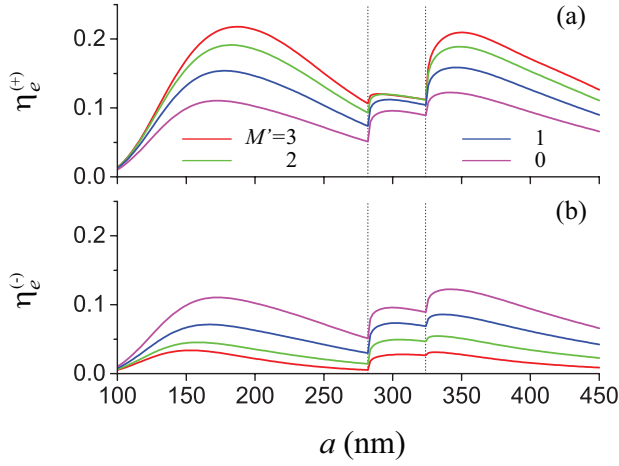


FIG. 17. (Color online) Directional fractional rates $\eta_e^{(f)} = \gamma_e^{(g,f)}/\gamma_e$ of spontaneous emission into guided modes in the (a) positive and (b) negative propagation directions as functions of the fiber radius a . The atom is positioned at the point $(r = a, \varphi = 0)$. The quantization axis z_Q coincides with the axis y . Other parameters are as for Fig. 2. The vertical dotted lines indicate the positions of the cutoffs for higher-order modes.

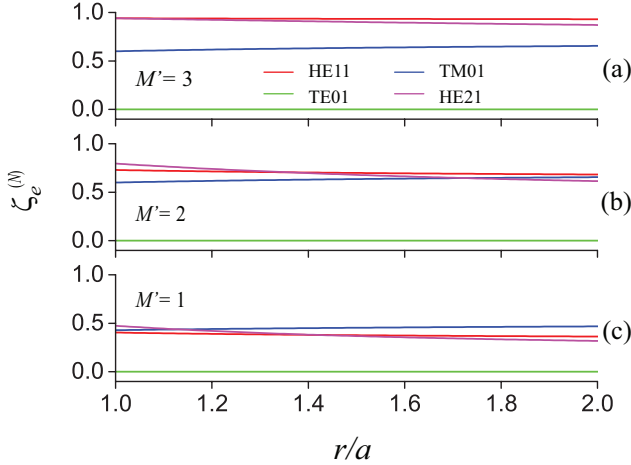


FIG. 18. (Color online) Radial dependencies of the asymmetry factors $\zeta_e^{(N)}$ for directional spontaneous emission from different magnetic sublevels of the hfs level $5P_{3/2}F' = 3$ into different guided modes. The atom is positioned on the positive side of the axis x and the quantization axis z_Q coincides with the axis y . Other parameters are as for Fig. 2.

of the fiber axis can be characterized by the factors

$$\zeta_e^{(N)} = \frac{\gamma_e^{(N+)} - \gamma_e^{(N-)}}{\gamma_e^{(N+)} + \gamma_e^{(N-)}}, \quad (31)$$

$$\zeta_e = \frac{\gamma_e^{(g+)} - \gamma_e^{(g-)}}{\gamma_e^{(g+)} + \gamma_e^{(g-)}}.$$

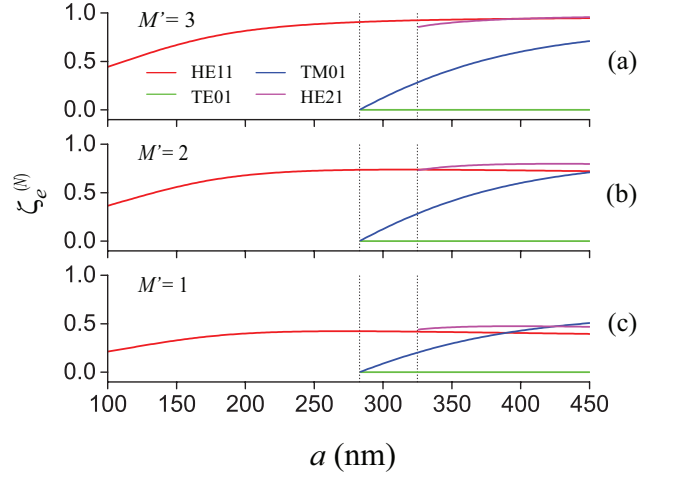


FIG. 19. (Color online) Asymmetry factors $\zeta_e^{(N)}$ for directional spontaneous emission from different magnetic sublevels of the hfs level $5P_{3/2}F' = 3$ into different guided modes as functions of the fiber radius a . The atom is positioned at the point $(r = a, \varphi = 0)$. The quantization axis z_Q coincides with the axis y . Other parameters are as for Fig. 2.

We note that $\zeta_{\bar{e}}^{(N)} = -\zeta_e^{(N)}$ and $\zeta_{\bar{e}} = -\zeta_e$. Hence, for the sublevel with $M' = 0$, we have $\zeta_e^{(N)} = \zeta_e = 0$.

We calculate numerically $\zeta_e^{(N)}$ for $|e\rangle$ with $M' > 0$. We show in Figs. 18 and 19 the asymmetry factors $\zeta_e^{(N)}$ for directional spontaneous emission into different guided modes as functions of the radial distance and the fiber radius. The atom is positioned on the positive side of the axis x and the quantization axis z_Q coincides with the axis y . We observe from Fig. 18 that $\zeta_e^{(N)}$ varies very slowly with increasing distance r . We see from Fig. 19 that $\zeta_e^{(N)}$ tends to reach a stationary value when the fiber radius a is large enough. It is interesting to note that $\zeta_e^{(N)} = 0$ for the TE₀₁ modes. The reason is that, since the longitudinal component $e_z^{(\mu)}$ of the electric part of a TE mode is zero, the profile function $\mathbf{e}^{(\mu)}$ of this mode does not depend on the propagation direction and, hence, neither does the rate for the corresponding channel of spontaneous emission.

The asymmetry between the rates of spontaneous emission into the positive and negative directions of the fiber axis depends on the orientation of the quantization axis with respect to the position of the atom. We show in Figs. 20 and 21 the directional asymmetry factors $\zeta_e^{(N)}$ of spontaneous emission into different guided modes as functions of the azimuthal angle φ_Q and the zenithal angle θ_Q of the quantization axis z_Q . In these calculations, we assumed that the atom is positioned at the point $(r = a, \varphi = 0)$.

We observe from Fig. 20 and 21 that, except for $M' = 3$ and $N = \text{TM}_{01}$, the absolute values of $\zeta_e^{(N)}$ are maximal when $\varphi_Q = \pi/2$ or $3\pi/2$ and $\theta_Q = \pi/2$. These angles correspond to the case where the quantization axis z_Q

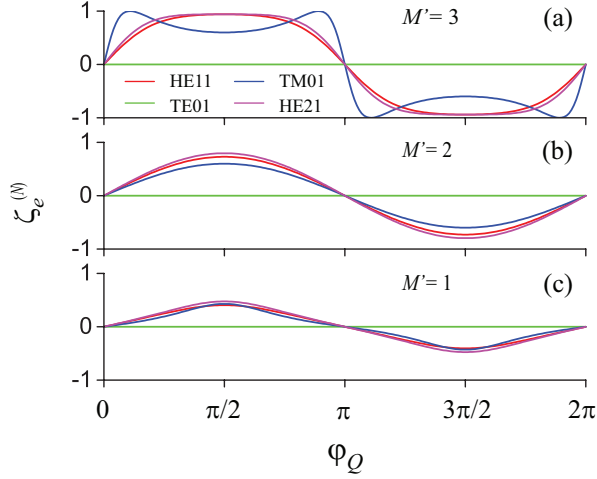


FIG. 20. (Color online) Asymmetry factors $\zeta_e^{(N)}$ for directional spontaneous emission from different magnetic sublevels of the hfs level $5P_{3/2}F' = 3$ into different guided modes as functions of the azimuthal angle φ_Q of the quantization axis z_Q . The zenithal angle of the axis z_Q is $\theta_Q = \pi/2$. The atom is positioned at the point ($r = a, \varphi = 0$). Other parameters are as for Fig. 2.

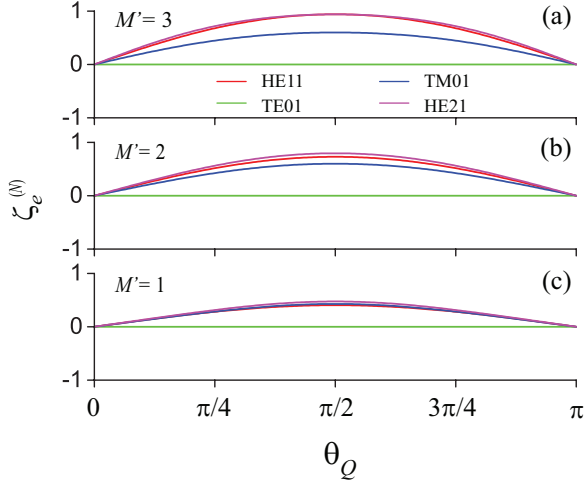


FIG. 21. (Color online) Asymmetry factors $\zeta_e^{(N)}$ for directional spontaneous emission from different magnetic sublevels of the hfs level $5P_{3/2}F' = 3$ into different guided modes as functions of the zenithal angle θ_Q of the quantization axis z_Q . The azimuthal angle of the axis z_Q is $\varphi_Q = \pi/2$. The atom is positioned at the point ($r = a, \varphi = 0$). Other parameters are as for Fig. 2.

coincides with the axis y . This axis is perpendicular to the meridional plane containing the position of the atom.

The blue curve in Fig. 20(a), which corresponds to $M' = 3$, $N = \text{TM}_{01}$, and $\theta_Q = \pi/2$, indicates that the absolute value of the asymmetry factor $\zeta_e^{(N)}$ is equal to 1 at four values $\varphi_Q = \varphi_0, \pi - \varphi_0, \pi + \varphi_0$, or $2\pi - \varphi_0$, where $\varphi_0 \simeq 0.108\pi \simeq 19^\circ$. This means that the spontaneous

emission from the outermost sublevel $|F' = 3, M' = 3\rangle$ of the hfs level $5P_{3/2}F' = 3$ into the TM modes is unidirectional when the quantization axis z_Q lies at an appropriate azimuthal angle φ_Q in the fiber transverse plane xy . This interesting feature arises as a consequence of the properties of the cyclic transition and the TM modes. Indeed, the only allowed electric dipole transition from the sublevel $|F' = 3, M' = 3\rangle$ of the excited state $5P_{3/2}$ is the σ_+ transition to the sublevel $|F = 2, M = 2\rangle$ of the ground state $5S_{1/2}$. The dipole of this transition is coupled to the counterclockwise circular component of the projection of the electric part of the field onto the plane $x_Q y_Q$, which is perpendicular to the quantization axis z_Q . When the quantization axis lies in the fiber transverse plane xy and is oriented at an azimuthal angle $\varphi_Q = \varphi_0, \pi - \varphi_0, \pi + \varphi_0$, or $2\pi - \varphi_0$, where $\varphi_0 = \arcsin(|e_z|/|e_r|)$, the polarization of the projection of the electric part of a TM mode onto the plane $x_Q y_Q$ is exactly circular at the position of the atom. The rotation direction of this polarization depends on the propagation direction f . Consequently, spontaneous emission from the sublevel $|F' = 3, M' = 3\rangle$ into the TM modes is unidirectional.

V. SUMMARY

In this work, we have studied spontaneous emission from a rubidium-87 atom into the fundamental and higher-order modes of a vacuum-clad ultrathin optical fiber. We have shown that the spontaneous emission rate depends on the magnetic sublevel, the type of modes, the orientation of the quantization axis, and the fiber radius. We have found that the rate of spontaneous emission into the TE modes is always symmetric with respect to the propagation directions. Meanwhile, the rates of spontaneous emission into other guided modes do not depend on the propagation direction when the quantization axis lies in the meridional plane containing the position of the atom. Asymmetry of spontaneous emission with respect to the propagation directions may appear when the output modes are not TE modes and the quantization axis does not lie in the meridional plane containing the position of the atom. We have shown that the rate of spontaneous emission into guided modes propagating in a given direction does not change when both the propagation direction and the magnetic quantum number are reversed. This result means that asymmetry of spontaneous emission with respect to the propagation directions leads to asymmetry with respect to the magnetic quantum numbers and vice versa. For the fiber radius in the range from 330 nm to 450 nm, the spontaneous emission into the HE₂₁ modes is stronger than into the HE₁₁, TE₀₁, and TM₀₁ modes. When the quantization axis coincides with the fiber axis and the radial distance is not too large, the rates of spontaneous emission from the outermost magnetic sublevels into guided modes are larger than those from the other sublevels. At the cutoff for higher-order modes, the rates of spontaneous emission into guided

and radiation modes undergo steep variations, which are caused by the changes of the mode structure. Due to the mutual compensation of these changes, the variations of the total rate of spontaneous emission into both types of modes are smooth. The total fractional rate of emission into guided modes is most substantial when the fiber radius is around 180 nm, where the fiber supports only the fundamental HE_{11} modes, or 340 nm, where the fiber supports not only the HE_{11} modes but also the TE_{01} , TM_{01} , and HE_{21} modes. We have shown that the spontaneous emission from the upper level up the cyclic transition into the TM modes is unidirectional when the quantization axis lies at an appropriate azimuthal angle in the fiber transverse plane. Our results lay the foundations for future research on manipulating and controlling the coupling of atoms, molecules, and dielectric particles to higher-order modes of ultrathin optical fibers.

ACKNOWLEDGMENTS

We acknowledge support for this work from the Okinawa Institute of Science and Technology Graduate University. S.N.C. and T.B. are grateful to JSPS for partial support from a Grant-in-Aid for Scientific Research (Grant No. 26400422).

Appendix A: Guided modes of a step-index fiber

Consider the model of a step-index fiber that is a dielectric cylinder of radius a and refractive index n_1 and is surrounded by an infinite background medium of refractive index n_2 , where $n_2 < n_1$. We use the Cartesian coordinates $\{x, y, z\}$, where z is the coordinate along the fiber axis. We also use the cylindrical coordinates $\{r, \varphi, z\}$, where r and φ are the polar coordinates in the fiber transverse plane xy .

For a guided light field of frequency ω (free-space wavelength $\lambda = 2\pi c/\omega$ and free-space wave number $k = \omega/c$), the propagation constant β is determined by the fiber eigenvalue equation [75]

$$\left[\frac{J'_l(ha)}{haJ_l(ha)} + \frac{K'_l(qa)}{qaK_l(qa)} \right] \left[\frac{n_1^2 J'_l(ha)}{haJ_l(ha)} + \frac{n_2^2 K'_l(qa)}{qaK_l(qa)} \right] = l^2 \left(\frac{1}{h^2 a^2} + \frac{1}{q^2 a^2} \right)^2 \frac{\beta^2}{k^2}. \quad (\text{A1})$$

Here, we have introduced the parameters $h = (n_1^2 k^2 - \beta^2)^{1/2}$ and $q = (\beta^2 - n_2^2 k^2)^{1/2}$, which characterize the scales of the spatial variations of the field inside and outside the fiber, respectively. The integer index $l = 0, 1, 2, \dots$ is the azimuthal mode order, which determines the helical phasefront and the associated phase gradient in the fiber transverse plane. The notations J_l and K_l stand for the Bessel functions of the first kind and the modified Bessel functions of the second kind, respectively.

The notations $J'_l(x)$ and $K'_l(x)$ stand for the derivatives of $J_l(x)$ and $K_l(x)$ with respect to the argument x .

For $l \geq 1$, the eigenvalue equation (A1) leads to hybrid HE and EH modes [75]. The eigenvalue equation is given, for HE modes, as

$$\frac{J_{l-1}(ha)}{haJ_l(ha)} = -\frac{n_1^2 + n_2^2}{2n_1^2} \frac{K'_l(qa)}{qaK_l(qa)} + \frac{l}{h^2 a^2} - \mathcal{R} \quad (\text{A2})$$

and, for EH modes, as

$$\frac{J_{l-1}(ha)}{haJ_l(ha)} = -\frac{n_1^2 + n_2^2}{2n_1^2} \frac{K'_l(qa)}{qaK_l(qa)} + \frac{l}{h^2 a^2} + \mathcal{R}. \quad (\text{A3})$$

Here, we have introduced the notation

$$\mathcal{R} = \left[\left(\frac{n_1^2 - n_2^2}{2n_1^2} \right)^2 \left(\frac{K'_l(qa)}{qaK_l(qa)} \right)^2 + \left(\frac{l\beta}{n_1 k} \right)^2 \left(\frac{1}{q^2 a^2} + \frac{1}{h^2 a^2} \right)^2 \right]^{1/2}. \quad (\text{A4})$$

We label HE and EH modes as HE_{lm} and EH_{lm} , respectively, where $l = 1, 2, \dots$ and $m = 1, 2, \dots$ are the azimuthal and radial mode orders, respectively. Here, the radial mode order m implies that the HE_{lm} or EH_{lm} mode is the m th solution to the corresponding eigenvalue equation (A2) or (A3), respectively.

For $l = 0$, the eigenvalue equation (A1) leads to TE and TM modes [75]. The eigenvalue equation is given, for TE modes, as

$$\frac{J_1(ha)}{haJ_0(ha)} = -\frac{K_1(qa)}{qaK_0(qa)} \quad (\text{A5})$$

and, for TM modes, as

$$\frac{J_1(ha)}{haJ_0(ha)} = -\frac{n_2^2}{n_1^2} \frac{K_1(qa)}{qaK_0(qa)}. \quad (\text{A6})$$

We label TE and TM modes as TE_{0m} and TM_{0m} , respectively, where $m = 1, 2, \dots$ is the radial mode order. The subscript 0 implies that the azimuthal mode order of TE and TM modes is $l = 0$. The radial mode order m implies that the TE_{0m} or TM_{0m} mode is the m th solution to the corresponding eigenvalue equation (A5) or (A6), respectively.

According to [75], the fiber size parameter V is defined as $V = ka\sqrt{n_1^2 - n_2^2}$. The cutoff values V_c for HE_{1m} modes are determined as solutions to the equation $J_1(V_c) = 0$. For HE_{lm} modes with $l = 2, 3, \dots$, the cutoff values are obtained as nonzero solutions to the equation $(n_1^2/n_2^2 + 1)(l-1)J_{l-1}(V_c) = V_c J_l(V_c)$. The cutoff values V_c for EH_{lm} modes, where $l = 1, 2, \dots$, are determined as nonzero solutions to the equation $J_l(V_c) = 0$. For TE_{0m} and TM_{0m} modes, the cutoff values V_c are obtained as solutions to the equation $J_0(V_c) = 0$.

The electric component of the field can be presented in the form

$$\mathbf{E} = \frac{1}{2} \mathcal{E} e^{-i\omega t} + \text{c.c.}, \quad (\text{A7})$$

where \mathcal{E} is the envelope. For a guided mode with a propagation constant β and an azimuthal mode order l , we can write

$$\mathcal{E} = \mathbf{e}e^{i\beta z + il\varphi}, \quad (\text{A8})$$

where \mathbf{e} is the mode profile function. In Eq. (A8), the parameters β and l can take not only positive but also negative values.

We decompose the vectorial function \mathbf{e} into the radial, azimuthal and axial components denoted by the subscripts r , φ and z , respectively. We summarize the expressions for the mode functions of hybrid modes, TE modes, and TM modes in the below [75].

1. Hybrid modes

We consider hybrid modes $N = \text{HE}_{lm}$ or EH_{lm} . It is convenient to introduce the parameter

$$s = l \left(\frac{1}{h^2 a^2} + \frac{1}{q^2 a^2} \right) \left[\frac{J'_l(ha)}{haJ_l(ha)} + \frac{K'_l(qa)}{qaK_l(qa)} \right]^{-1}. \quad (\text{A9})$$

Then, we find, for $r < a$,

$$\begin{aligned} e_r &= iA \frac{\beta}{2h} [(1-s)J_{l-1}(hr) - (1+s)J_{l+1}(hr)], \\ e_\varphi &= -A \frac{\beta}{2h} [(1-s)J_{l-1}(hr) + (1+s)J_{l+1}(hr)], \\ e_z &= AJ_l(hr), \end{aligned} \quad (\text{A10})$$

and, for $r > a$,

$$\begin{aligned} e_r &= iA \frac{\beta}{2q} \frac{J_l(ha)}{K_l(qa)} [(1-s)K_{l-1}(qr) + (1+s)K_{l+1}(qr)], \\ e_\varphi &= -A \frac{\beta}{2q} \frac{J_l(ha)}{K_l(qa)} [(1-s)K_{l-1}(qr) - (1+s)K_{l+1}(qr)], \\ e_z &= A \frac{J_l(ha)}{K_l(qa)} K_l(qr). \end{aligned} \quad (\text{A11})$$

Here, the parameter A is a constant that can be determined from the propagating power of the field. Without loss of generality, we take A to be a real number.

In the cylindrical coordinates, the mode profile function of the electric component of a quasicircularly polarized hybrid mode N with a propagation direction $f = \pm$ and a phase circulation direction $p = \pm$ is given by

$$\mathbf{e}^{(\omega N f p)} = \hat{\mathbf{r}}e_r + p\hat{\boldsymbol{\varphi}}e_\varphi + f\hat{\mathbf{z}}e_z, \quad (\text{A12})$$

where the mode function components e_r , e_φ , and e_z are given by Eqs. (A10) and (A11) for $\beta > 0$ and $l > 0$. These components depend explicitly on the azimuthal mode order l and implicitly on the radial mode order m . An important property of the mode functions of hybrid modes is that the longitudinal component e_z is nonvanishing and in quadrature ($\pi/2$ out of phase) with the radial component e_r . In addition, the azimuthal component e_φ is also nonvanishing and in quadrature with

the radial component e_r . We note that the full mode function of the quasicircularly polarized hybrid mode is $\mathcal{E}^{(\omega N f p)} = \mathbf{e}^{(\omega N f p)} e^{i\beta z + ipl\varphi}$, where $\beta > 0$ and $l > 0$.

We have the following symmetry relations:

$$\begin{aligned} e_r^{(\omega N f p)} &= e_r^{(\omega N \bar{f} p)} = e_r^{(\omega N f \bar{p})}, \\ e_\varphi^{(\omega N f p)} &= e_\varphi^{(\omega N \bar{f} p)} = -e_\varphi^{(\omega N f \bar{p})}, \\ e_z^{(\omega N f p)} &= -e_z^{(\omega N \bar{f} p)} = e_z^{(\omega N f \bar{p})}, \end{aligned} \quad (\text{A13})$$

and

$$e_r^{(\mu)*} = -e_r^{(\mu)}, \quad e_\varphi^{(\mu)*} = e_\varphi^{(\mu)}, \quad e_z^{(\mu)*} = e_z^{(\mu)}, \quad (\text{A14})$$

where $\bar{f} = -f$ and $\bar{p} = -p$. From Eqs. (A13) and (A14), we obtain the formulas

$$\begin{aligned} e_r^{(\omega N f p)} &= -e_r^{(\omega N \bar{f} \bar{p})*}, \\ e_\varphi^{(\omega N f p)} &= -e_\varphi^{(\omega N \bar{f} \bar{p})*}, \\ e_z^{(\omega N f p)} &= -e_z^{(\omega N \bar{f} \bar{p})*}, \end{aligned} \quad (\text{A15})$$

which yield

$$\mathbf{e}^{(\omega N f p)} = -\mathbf{e}^{(\omega N \bar{f} \bar{p})*}. \quad (\text{A16})$$

Equation (A16) is a consequence of the time reversal symmetry of the field.

2. TE modes

We consider transverse electric modes $N = \text{TE}_{0m}$. For $r < a$, we have

$$\begin{aligned} e_r &= 0, \\ e_\varphi &= i \frac{\omega \mu_0}{h} A J_1(hr), \\ e_z &= 0. \end{aligned} \quad (\text{A17})$$

For $r > a$, we have

$$\begin{aligned} e_r &= 0, \\ e_\varphi &= -i \frac{\omega \mu_0}{q} \frac{J_0(ha)}{K_0(qa)} A K_1(qr), \\ e_z &= 0. \end{aligned} \quad (\text{A18})$$

Without loss of generality, we take A to be a real number.

The mode profile function of the electric component of a TE_{0m} mode with a propagation direction $f = \pm$ can be written as

$$\mathbf{e}^{(\omega \text{TE}_{0m} f)} = \hat{\boldsymbol{\varphi}}e_\varphi, \quad (\text{A19})$$

where the only nonzero cylindrical component e_φ is given by the second expressions in Eqs. (A17) and (A18). The mode function depends implicitly on the radial mode order m . The full mode function of the TE mode is $\mathcal{E}^{(\omega \text{TE}_{0m} f)} = \mathbf{e}^{(\omega \text{TE}_{0m} f)} e^{i\beta z}$, where $\beta > 0$.

We find the relations

$$e_\varphi^{(\omega \text{TE}_{0m} f)} = e_\varphi^{(\omega \text{TE}_{0m} \bar{f})} = -e_\varphi^{(\omega \text{TE}_{0m} f)*}, \quad (\text{A20})$$

which yield

$$\mathbf{e}^{(\omega \text{TE}_{0m} f)} = -\mathbf{e}^{(\omega \text{TE}_{0m} \bar{f})*}. \quad (\text{A21})$$

3. TM modes

We consider transverse magnetic modes $N = \text{TM}_{0m}$. For $r < a$, we have

$$\begin{aligned} e_r &= -i\frac{\beta}{h}AJ_1(hr), \\ e_\varphi &= 0, \\ e_z &= AJ_0(hr). \end{aligned} \quad (\text{A22})$$

For $r > a$, we have

$$\begin{aligned} e_r &= i\frac{\beta}{q}\frac{J_0(ha)}{K_0(qa)}AK_1(qr), \\ e_\varphi &= 0, \\ e_z &= \frac{J_0(ha)}{K_0(qa)}AK_0(qr). \end{aligned} \quad (\text{A23})$$

Without loss of generality, we take A to be a real number.

The mode profile function of the electric component of a TM mode with a propagation direction $f = \pm$ can be written as

$$\mathbf{e}^{(\omega\text{TM}_{0m}f)} = \hat{\mathbf{r}}e_r + f\hat{\mathbf{z}}e_z, \quad (\text{A24})$$

where the components e_r and e_z are given by the first and third expressions in Eqs. (A22) and (A23) for $\beta > 0$. The mode function depends implicitly on the radial mode order m . Like the case of hybrid modes, the longitudinal component e_z of a TM mode is nonvanishing and in quadrature ($\pi/2$ out of phase) with the radial component e_r . The full mode function of the TM mode is $\mathcal{E}^{(\omega\text{TM}_{0m}f)} = \mathbf{e}^{(\omega\text{TM}_{0m}f)}e^{if\beta z}$, where $\beta > 0$.

We find the relations

$$\begin{aligned} e_r^{(\omega\text{TM}_{0m}f)} &= e_r^{(\omega\text{TM}_{0m}\bar{f})} = -e_r^{(\omega\text{TM}_{0m}f)*}, \\ e_z^{(\omega\text{TM}_{0m}f)} &= -e_z^{(\omega\text{TM}_{0m}\bar{f})} = e_z^{(\omega\text{TM}_{0m}f)*}, \end{aligned} \quad (\text{A25})$$

which yield

$$\mathbf{e}^{(\omega\text{TM}_{0m}f)} = -\mathbf{e}^{(\omega\text{TM}_{0m}\bar{f})*}. \quad (\text{A26})$$

Appendix B: Radiation modes of a nanofiber

We present the electric component of the field in the form $\mathbf{E} = (1/2)(\mathcal{E}e^{-i\omega t} + \text{c.c.})$, where \mathcal{E} is the envelope. For a radiation mode with a propagation constant β in the range $-kn_2 < \beta < kn_2$ and a mode order $l = 0, \pm 1, \pm 2, \dots$, we can write $\mathcal{E} = \mathbf{e}e^{i\beta z + il\varphi}$, where \mathbf{e} is the mode profile function. The characteristic parameters for the field in the inside and outside of the fiber are $h = \sqrt{k^2n_1^2 - \beta^2}$ and $q = \sqrt{k^2n_2^2 - \beta^2}$, respectively.

The mode functions of the electric parts of the radiation modes $\nu = (\omega\beta l p)$ [75] are given, for $r < a$, by

$$\begin{aligned} e_r^{(\nu)} &= \frac{i}{h^2} \left[\beta h A J_l'(hr) + il \frac{\omega\mu_0}{r} B J_l(hr) \right], \\ e_\varphi^{(\nu)} &= \frac{i}{h^2} \left[il \frac{\beta}{r} A J_l(hr) - h\omega\mu_0 B J_l'(hr) \right], \\ e_z^{(\nu)} &= A J_l(hr), \end{aligned} \quad (\text{B1})$$

and, for $r > a$, by

$$\begin{aligned} e_r^{(\nu)} &= \frac{i}{q^2} \sum_{j=1,2} \left[\beta q C_j H_l^{(j)'}(qr) + il \frac{\omega\mu_0}{r} D_j H_l^{(j)}(qr) \right], \\ e_\varphi^{(\nu)} &= \frac{i}{q^2} \sum_{j=1,2} \left[il \frac{\beta}{r} C_j H_l^{(j)}(qr) - q\omega\mu_0 D_j H_l^{(j)'}(qr) \right], \\ e_z^{(\nu)} &= \sum_{j=1,2} C_j H_l^{(j)}(qr). \end{aligned} \quad (\text{B2})$$

Here, A and B as well as C_j and D_j with $j = 1, 2$ are coefficients. The coefficients C_j and D_j are related to the coefficients A and B as [45]

$$\begin{aligned} C_j &= (-1)^j \frac{i\pi q^2 a}{4n_2^2} (AL_j + i\mu_0 c B V_j), \\ D_j &= (-1)^{j-1} \frac{i\pi q^2 a}{4} (i\epsilon_0 c AV_j - B M_j), \end{aligned} \quad (\text{B3})$$

where

$$\begin{aligned} V_j &= \frac{lk\beta}{ah^2q^2} (n_2^2 - n_1^2) J_l(ha) H_l^{(j)*}(qa), \\ M_j &= \frac{1}{h} J_l'(ha) H_l^{(j)*}(qa) - \frac{1}{q} J_l(ha) H_l^{(j)*'}(qa), \\ L_j &= \frac{n_1^2}{h} J_l'(ha) H_l^{(j)*}(qa) - \frac{n_2^2}{q} J_l(ha) H_l^{(j)*'}(qa). \end{aligned} \quad (\text{B4})$$

We specify two polarizations by choosing $B = i\eta A$ and $B = -i\eta A$ for $p = +$ and $p = -$, respectively. We take A to be a real number. The orthogonality of the modes requires

$$\begin{aligned} \int_0^{2\pi} d\varphi \int_0^\infty n_{\text{ref}}^2 \left[\mathbf{e}^{(\nu)} \mathbf{e}^{(\nu')*} \right]_{\beta=\beta', l=l'} r dr \\ = N_\nu \delta_{pp'} \delta(\omega - \omega'). \end{aligned} \quad (\text{B5})$$

This leads to

$$\eta = \epsilon_0 c \sqrt{\frac{n_2^2 |V_j|^2 + |L_j|^2}{|V_j|^2 + n_2^2 |M_j|^2}}. \quad (\text{B6})$$

The constant N_ν is given by

$$N_\nu = \frac{8\pi\omega}{q^2} \left(n_2^2 |C_j|^2 + \frac{\mu_0}{\epsilon_0} |D_j|^2 \right). \quad (\text{B7})$$

We introduce the notations $\bar{\beta} = -\beta$, $\bar{l} = -l$, and $\bar{p} = -p$. We find the symmetry relations

$$\begin{aligned} e_r^{(\omega\beta l p)} &= -e_r^{(\omega\bar{\beta}\bar{l}\bar{p})}, \\ e_\varphi^{(\omega\beta l p)} &= -e_\varphi^{(\omega\bar{\beta}\bar{l}\bar{p})}, \\ e_z^{(\omega\beta l p)} &= e_z^{(\omega\bar{\beta}\bar{l}\bar{p})}, \end{aligned} \quad (\text{B8})$$

$$\begin{aligned} e_r^{(\omega\beta l p)} &= (-1)^l e_r^{(\omega\beta\bar{l}\bar{p})}, \\ e_\varphi^{(\omega\beta l p)} &= (-1)^{l+1} e_\varphi^{(\omega\beta\bar{l}\bar{p})}, \\ e_z^{(\omega\beta l p)} &= (-1)^l e_z^{(\omega\beta\bar{l}\bar{p})}, \end{aligned} \quad (\text{B9})$$

and

$$e_r^{(\nu)*} = -e_r^{(\nu)}, \quad e_\varphi^{(\nu)*} = e_\varphi^{(\nu)}, \quad e_z^{(\nu)*} = e_z^{(\nu)}, \quad (\text{B10})$$

which yield

$$\mathbf{e}^{(\omega\beta lp)} = (-1)^l \mathbf{e}^{(\omega\beta \bar{l} p)*}. \quad (\text{B11})$$

For the spherical tensor components $e_q^{(\omega, \beta, l, p)}$, with the index $q = 0, \pm 1$, of the radiation mode functions, we find the relations

$$e_q^{(\omega\beta lp)} = (-1)^q e_q^{(\omega\beta \bar{l} p)}, \quad (\text{B12})$$

$$e_q^{(\omega\beta lp)} = (-1)^{l+q} e^{2iq\varphi} e_{-q}^{(\omega\beta \bar{l} p)}, \quad (\text{B13})$$

and

$$e_q^{(\omega\beta lp)} = (-1)^q e^{2iq\varphi} e_q^{(\omega\beta lp)*}. \quad (\text{B14})$$

-
- [1] L. Tong, R. R. Gattass, J. B. Ashcom, S. He, J. Lou, M. Shen, I. Maxwell, and E. Mazur, *Nature (London)* **426**, 816 (2003).
- [2] T. A. Birks, W. J. Wadsworth, and P. St. J. Russell, *Opt. Lett.* **25**, 1415 (2000); S. G. Leon-Saval, T. A. Birks, W. J. Wadsworth, P. St. J. Russell, and M. W. Mason, in *Conference on Lasers and Electro-Optics (CLEO), Technical Digest*, postconference ed. (Optical Society of America, Washington, D.C., 2004), paper CPDA6.
- [3] J. C. Knight, G. Cheung, F. Jacques, and T. A. Birks, *Opt. Lett.* **22**, 1129 (1997); M. Cai and K. Vahala, *ibid.* **26**, 884 (2001).
- [4] J. Bures and R. Ghosh, *J. Opt. Soc. Am. A* **19**, 1992 (1999).
- [5] L. Tong, J. Lou, and E. Mazur, *Opt. Express* **12**, 1025 (2004).
- [6] Fam Le Kien, J. Q. Liang, K. Hakuta, and V. I. Balykin, *Opt. Commun.* **242**, 445 (2004).
- [7] M. J. Morrissey, K. Deasy, M. Frawley, R. Kumar, E. Prel, L. Russell, V. G. Truong, and S. Nic Chormaic, *Sensors* **13**, 10449 (2013).
- [8] T. Nieddu, V. Gokhroo, and S. Nic Chormaic, *J. Opt.* **18**, 053001 (2016).
- [9] V. I. Balykin, K. Hakuta, Fam Le Kien, J. Q. Liang, and M. Morinaga, *Phys. Rev. A* **70**, 011401(R) (2004); Fam Le Kien, V. I. Balykin, and K. Hakuta, *ibid.* **70**, 063403 (2004).
- [10] E. Vetsch, D. Reitz, G. Sagué, R. Schmidt, S. T. Dawkins, and A. Rauschenbeutel, *Phys. Rev. Lett.* **104**, 203603 (2010).
- [11] A. Goban, K. S. Choi, D. J. Alton, D. Ding, C. Lacroûte, M. Pototschnig, T. Thiele, N. P. Stern, and H. J. Kimble, *Phys. Rev. Lett.* **109**, 033603 (2012).
- [12] P. Domokos, P. Horak, and H. Ritsch, *Phys. Rev. A* **65**, 033832 (2002).
- [13] Fam Le Kien, V. I. Balykin, and K. Hakuta, *Phys. Rev. A* **73**, 013819 (2006).
- [14] K. P. Nayak, P. N. Melentiev, M. Morinaga, Fam Le Kien, V. I. Balykin, and K. Hakuta, *Opt. Express* **15**, 5431 (2007).
- [15] K. P. Nayak, Fam Le Kien, M. Morinaga, and K. Hakuta, *Phys. Rev. A* **79**, 021801(R) (2009).
- [16] M. J. Morrissey, K. Deasy, Y. Wu, S. Chakrabarti, and S. Nic Chormaic, *Rev. Sci. Instrum.* **80**, 053102 (2009).
- [17] S. T. Dawkins, R. Mitsch, D. Reitz, E. Vetsch, and A. Rauschenbeutel, *Phys. Rev. Lett.* **107**, 243601 (2011).
- [18] D. Reitz, C. Sayrin, R. Mitsch, P. Schneeweiss, and A. Rauschenbeutel, *Phys. Rev. Lett.* **110**, 243603 (2013).
- [19] L. Russell, R. Kumar, V. B. Tiwari, and S. Nic Chormaic, *Opt. Commun.* **309**, 313 (2013).
- [20] R. Kumar, V. Gokhroo, V. B. Tiwari, and S. Nic Chormaic, *J. Opt.* **18**, 115401, (2016).
- [21] A. Stiebeiner, O. Rehband, R. Garcia-Fernandez, and A. Rauschenbeutel, *Opt. Express* **17**, 21704 (2009).
- [22] R. Yalla, Fam Le Kien, M. Morinaga, and K. Hakuta, *Phys. Rev. Lett.* **109**, 063602 (2012).
- [23] T. Schröder, M. Fujiwara, T. Noda, H.-Q. Zhao, O. Benson, and S. Takeuchi, *Opt. Express* **20**, 10490 (2012).
- [24] L. Liebermeister, F. Petersen, A. V. Münchow, D. Burchardt, J. Hermelbracht, T. Tashima, A. W. Schell, O. Benson, T. Meinhardt, A. Krueger, A. Stiebeiner, A. Rauschenbeutel, H. Weinfurter, and M. Weber, *Appl. Phys. Lett.* **104**, 031101 (2014).
- [25] G. Brambilla, G. S. Murugan, J. S. Wilkinson, and D. J. Richardson, *Opt. Lett.* **32**, 3041 (2007).
- [26] S. E. Skelton, M. Sergides, R. Patel, E. Karczewska, O. M. Maragó, and P. H. Jones, *J. Quant. Spectrosc. Radiat. Transfer* **113**, 2512 (2012).
- [27] Fam Le Kien and A. Rauschenbeutel, *Phys. Rev. A* **88**, 063845 (2013).
- [28] J. Fu, X. Yin, and L. Tong, *J. Phys. B: At. Mol. Opt. Phys.* **40**, 4195 (2007).
- [29] G. Sagué, A. Baade, and A. Rauschenbeutel, *New J. Phys.* **10**, 113008 (2008).
- [30] J. Fu, X. Yin, N. Li, and L. Tong, *Chinese Opt. Lett.* **112** (2008).
- [31] A. V. Masalov and V. G. Minogin, *Laser Phys. Lett.* **10**, 075203 (2013).
- [32] C. F. Phelan, T. Hennessy, and T. Busch, *Opt. Express* **21**, 27093 (2013).
- [33] M. Sadgrove, S. Wimberger, and S. Nic Chormaic, *Sci. Rep.* **6**, 28905 (2016).
- [34] M. H. Alizadeh and B. M. Reinhard, *Opt. Lett.* **41**, 4735 (2016).
- [35] G. Volpe and D. Petrov, *Opt. Commun.* **237**, 89 (2004).
- [36] A. Petcu-Colan, M. Frawley, and S. Nic Chormaic, *J. Nonlinear Opt. Phys. Mat.* **20**, 293 (2011).
- [37] M. C. Frawley, A. Petcu-Colan, V. G. Truong, and S. Nic Chormaic, *Opt. Commun.* **285**, 4648 (2012).
- [38] S. Ravets, J. E. Hoffman, L. A. Orozco, S. L. Rolston, G. Beadie, and F. K. Fatemi, *Opt. Express* **21**, 18325 (2013).

- [39] J. M. Ward, A. Maimaiti, V. H. Le, and S. Nic Chormaic, *Rev. Sci. Instrum.* **85**, 111501 (2014).
- [40] R. Kumar, V. Gokhroo, K. Deasy, A. Maimaiti, M. C. Frawley, C. Phelan, and S. Nic Chormaic, *New. J. Phys.* **17**, 013026 (2015).
- [41] A. Maimaiti, Viet Giang Truong, M. Sergides, I. Gusachenko, and S. Nic Chormaic, *Sci. Rep.* **5**, 09077 (2015).
- [42] A. Maimaiti, D. Holzmann, Viet Giang Truong, H. Ritsch, and S. Nic Chormaic, *Sci. Rep.* **6**, 30131 (2016).
- [43] H. Nha and W. Jhe, *Phys. Rev. A* **56**, 2213 (1997).
- [44] V. V. Klimov and M. Ducloy, *Phys. Rev. A* **69**, 013812 (2004).
- [45] T. Søndergaard and B. Tromborg, *Phys. Rev. A* **64**, 033812 (2001).
- [46] Fam Le Kien, S. Dutta Gupta, V. I. Balykin, and K. Hakuta, *Phys. Rev. A* **72**, 032509 (2005).
- [47] Fam Le Kien and K. Hakuta, *Phys. Rev. A* **78**, 063803 (2008).
- [48] See S. Chang and V. Minogin, *Phys. Rep.* **365**, 65 (2002), and references therein.
- [49] S.-Y. Lee, I.-M. Lee, J. Park, S. Oh, W. Lee, K.-Y. Kim, and B. Lee, *Phys. Rev. Lett.* **108**, 213907 (2012).
- [50] J. Lin, J. P. B. Mueller, Q. Wang, G. Yuan, N. Antoniou, X.-C. Yuan, and F. Capasso, *Science* **340**, 331 (2013).
- [51] F. J. Rodriguez-Fortuño, G. Marino, P. Ginzburg, D. O'Connor, A. Martinez, G. A. Wurtz, and A. V. Zayats, *Science* **340**, 328 (2013).
- [52] J. P. B. Mueller and F. Capasso, *Phys. Rev. B* **88**, 121410 (2013).
- [53] Z. Xi, Y. Lu, P. Yao, W. Yu, P. Wang, and H. Ming, *Opt. Express* **21**, 30327 (2013).
- [54] M. Neugebauer, T. Bauer, P. Banzer, and G. Leuchs, *Nano Lett.* **14**, 2546 (2014).
- [55] M. Neugebauer, T. Bauer, A. Aiello, P. Banzer, *Phys. Rev. Lett.* **114**, 063901 (2015).
- [56] F. J. Rodriguez-Fortuño, N. Engheta, A. Martinez, and A. V. Zayats, *Nature Commun.* **6**, 8799 (2015).
- [57] S. Sukhov, V. Kajorndejnukul, R. R. Naraghi, and A. Dogariu, *Nature Photon.* **9**, 809 (2015).
- [58] Fam Le Kien and A. Rauschenbeutel, *Phys. Rev. A* **90**, 023805 (2014).
- [59] J. Petersen, J. Volz, and A. Rauschenbeutel, *Science* **346**, 67 (2014).
- [60] R. Mitsch, C. Sayrin, B. Albrecht, P. Schneeweiss, and A. Rauschenbeutel, *Nature Commun.* **5**, 5713 (2014).
- [61] Fam Le Kien and A. Rauschenbeutel, *Phys. Rev. A* **90**, 063816 (2014).
- [62] S. Scheel, S. Y. Buhmann, C. Clausen, and P. Schneeweiss, *Phys. Rev. A* **92**, 043819 (2015).
- [63] C. Sayrin, C. Junge, R. Mitsch, B. Albrecht, D. O'Shea, P. Schneeweiss, J. Volz, and A. Rauschenbeutel, *Phys. Rev. X* **5**, 041036 (2015).
- [64] A. V. Dooghin, N. D. Kundikova, V. S. Liberman, and B. Y. Zeldovich, *Phys. Rev. A* **45**, 8204 (1992); V. S. Liberman and B. Y. Zeldovich, *Phys. Rev. A* **46**, 5199 (1992); M. Y. Darsht, B. Y. Zeldovich, I. V. Kataevskaya, and N. D. Kundikova, *JETP* **80**, 817 (1995) [*Zh. Eksp. Theor. Phys.* **107**, 1464 (1995)].
- [65] K. Y. Bliokh, A. Aiello, and M. A. Alonso, in *The Angular Momentum of Light*, edited by D. L. Andrews and M. Babiker (Cambridge University Press, New York, 2012), p. 174.
- [66] K. Y. Bliokh, A. Y. Bekshaev, and F. Nori, *Nature Commun.* **5**, 3300 (2014).
- [67] K. Y. Bliokh, F. J. Rodriguez-Fortuño, F. Nori, and A. V. Zayats, *Nature Photon.* **9**, 796 (2015).
- [68] K. Y. Bliokh and F. Nori, *Phys. Rep.* **592**, 1 (2015).
- [69] A. Aiello, P. Banzer, M. Neugebauer, and G. Leuchs, *Nature Photon.* **9**, 789 (2015).
- [70] P. Lodahl, S. Mahmoodian, S. Stobbe, P. Schneeweiss, J. Volz, A. Rauschenbeutel, H. Pichler, and P. Zoller, *Nature* **541**, 473 (2017).
- [71] A. V. Masalov and V. G. Minogin, *Zh. Eksp. Teor. Fiz.* **145**, 816 (2014).
- [72] H. J. Metcalf and P. van der Straten, *Laser Cooling and Trapping* (Springer, New York, 1999).
- [73] See, for example, B. W. Shore, *The Theory of Coherent Atomic Excitation* (Wiley, New York, 1990).
- [74] C. M. Caves and D. D. Crouch, *J. Opt. Soc. Am. B* **4**, 1535 (1987); K. J. Blow, R. Loudon, S. J. D. Phoenix, and T. J. Shepherd, *Phys. Rev. A* **42**, 4102 (1990).
- [75] See, for example, D. Marcuse, *Light Transmission Optics* (Krieger, Malabar, FL, 1989); A. W. Snyder and J. D. Love, *Optical Waveguide Theory* (Chapman and Hall, New York, 1983); K. Okamoto, *Fundamentals of Optical Waveguides* (Elsevier, New York, 2006).
- [76] Fam Le Kien, Th. Busch, Viet Giang Truong, and S. Nic Chormaic, *ArXiv*: 1703.00109.
- [77] V. Milner and Y. Prior, *Phys. Rev. Lett.* **80**, 940 (1998).
- [78] V. Milner, B. M. Chernobrod, and Y. Prior, *Phys. Rev. A* **60**, 1293 (1999).
- [79] A. V. Taichenachev, A. M. Tumaikin, and V. I. Yudin, *Europhys. Lett.* **45**, 301 (1999).
- [80] N. V. Vitanov, Z. Kis, and B. W. Shore, *Phys. Rev. A* **68**, 063414 (2003).
- [81] A. V. Taichenachev, A. M. Tumaikin, V. I. Yudin, and G. Nienhuis, *Phys. Rev. A* **69**, 033410 (2004).
- [82] V. I. Yudin, M. Yu. Basalaev, D. V. Brazhnikov, and A. V. Taichenachev, *Phys. Rev. A* **88**, 023862 (2013).
- [83] Fam Le Kien and A. Rauschenbeutel, *Phys. Rev. A* **93**, 043828 (2016).